

Structural and functional analysis of LIM domain-dependent recruitment of paxillin to focal adhesions

Marta Ripamonti

University of Geneva <https://orcid.org/0000-0002-1975-7930>

Nicolas Liaudet

Université de Genève, Faculty of Medicine

Bernhard Wehrle-Haller (✉ Bernhard.Wehrle-Haller@unige.ch)

University of Geneva <https://orcid.org/0000-0002-1159-1147>

Article

Keywords: BiFC, Cross-linking, Dynamics, Fibroblasts, Focal adhesion isolation, Half-life, LD motifs, Nanoscale orientation, Palmitoylation, Photoactivation, Phosphorylation, Plasma membrane, Replacement, Talin, Vinculin

Posted Date: August 21st, 2020

DOI: <https://doi.org/10.21203/rs.3.rs-42943/v1>

License: © ⓘ This work is licensed under a Creative Commons Attribution 4.0 International License.

[Read Full License](#)

Version of Record: A version of this preprint was published at Communications Biology on March 29th, 2021. See the published version at <https://doi.org/10.1038/s42003-021-01886-9>.

1 **Structural and functional analysis of LIM domain-dependent** 2 **recruitment of paxillin to focal adhesions**

3 Marta Ripamonti¹, Nicolas Liaudet² and Bernhard Wehrle-Haller^{1*}

4 ¹ Department of Cell Physiology and Metabolism, University of Geneva, Centre Médical
5 Universitaire, Rue Michel-Servet 1, 1211 Geneva 4, Switzerland.

6 ² Bioimaging Core Facility, Faculty of Medicine, University of Geneva, 1211 Geneva 4, Switzerland.

7 *Corresponding author, Bernhard.Wehrle-Haller@unige.ch.

8 **Key words**

9 BiFC; Cross-linking; Dynamics; Fibroblasts; Focal adhesion isolation; Half-life; LD motifs;
10 Nanoscale orientation; Palmitoylation; Photoactivation; Phosphorylation; Plasma membrane;
11 Replacement; Talin; Vinculin.

12 **Abstract**

13 The LIM domain-dependent localization of the adapter protein paxillin to focal adhesions (FAs) is
14 not mechanistically understood. Here, by combining molecular biology with photoactivation and FA-
15 isolation experiments, we demonstrate a specific contribution of each LIM domain and reveal the
16 existence of multiple paxillin docking sites in the FA-complex. Mutation of $\beta 3$ integrin at a putative
17 paxillin binding site leads to rapid inward sliding of FAs, correlating with enhanced paxillin
18 dissociation rates. Mechanical coupling of paxillin to integrins or the plasma membrane arrests the
19 FAs sliding, thereby disclosing an essential structural function of the LIM-array for the maturation of
20 integrin/talin clusters. Moreover, *via* bimolecular fluorescence complementation, we determine a
21 precise spatial orientation of the paxillin LIM domains, juxtaposing the positively charged LIM4 to
22 the plasma membrane and the extremity of the $\beta 3$ integrin tail, providing structural insights into the
23 molecular organization of FAs.

24 **Introduction**

25 The anchoring of cells to the extracellular matrix (ECM) is a critical function of integrins. Yet, these
26 heterodimeric receptors are also biomechanical sensors that trigger different signaling pathways in
27 response to extracellular stimuli ^{1,2}. To accomplish these mechanical and signaling functions, upon
28 ligand binding, integrins cluster in the plasma membrane (PM) and recruit the cytoplasmic adapter
29 proteins talin and kindlin ^{1,3-5}. Following the mechanical coupling to the actin cytoskeleton, notably
30 through the binding of the C-terminal domain of talin, signaling adapter proteins, such as paxillin and
31 FAK, are recruited to form nascent adhesions ⁶⁻⁸. Further maturation of these complexes into larger
32 focal adhesions (FAs) occurs in response to additional tension ⁹ and recruitment of reinforcing adapter
33 proteins, such as vinculin, that further cross-link talin to the actin cytoskeleton ^{10,11}.

34 Paxillin, contains in its N-terminal domain a proline-rich SH3-binding site ¹² and five LD motifs,
35 acting as discrete protein-binding domains, responsible for interaction with structural proteins, such
36 as vinculin, talin and the ILK/Pinch/parvin complex ^{10,13-16}. In addition, the LD motifs bind and recruit
37 signaling components such as kinases (e.g. FAK) and small GTPases to focal adhesions to control
38 the polymerization of the actin cytoskeleton ^{17,18}. The activity of the LD motifs, and notably the
39 association with FAK and vinculin, is controlled by numerous phosphorylation sites (Tyr, Ser, Thr),
40 which make paxillin an essential hub in the assembly of FAs and a pivotal player in coordinating
41 integrin-downstream signaling pathways ^{10,19,20}.

42 On the other hand, the paxillin C-terminus is composed of four highly similar LIM domains, that
43 constitute the FA targeting motif ²¹. Each LIM domain consists of two contiguous zinc-fingers,
44 stacked together through a shared hydrophobic core ^{22,23}, and mediates protein-protein interactions,
45 to create scaffolds for the assembly of multiprotein complexes at defined cellular sites ²⁴⁻²⁹. Structural
46 information of individual LIM domains revealed specific sites of interactions, as for example between
47 the ankyrin repeats of ILK and the first LIM domain of Pinch ²³. Although the biochemical and
48 structural nature of most of the proposed LIM domain-mediated interactions is not yet defined and
49 potentially spread over several LIM domains, many proteins containing multiple LIM domains are
50 recruited to FAs under mechanical tension ³⁰⁻³². It was therefore postulated that LIM domains could
51 function as tension sensors ³² and proposed that could act as a localizer, targeting proteins to specific
52 subcellular locations, such as tensioned or injured F-actin networks ^{22,32-34}. In the case of the paxillin
53 protein, a LIM3-, and partially LIM2-, dependent FA localization was proposed on the basis of
54 truncations and site-specific mutagenesis experiments ²¹. Additional work in paxillin- and Hic-5-null
55 embryonic stem cells, further confirmed this notion, proposing that LIM1 and LIM4 only marginally
56 contribute to FA-targeting ³⁵. Recently, different kindlin-dependent mechanisms of paxillin

57 recruitment to FAs were proposed³⁶⁻³⁸. However, in attached talin-deficient cells, paxillin remained
58 diffuse in the cytoplasm³⁹, suggesting that kindlin may not be the only determinant for paxillin
59 recruitment to FAs. Some reports have shown a direct binding of LIM domain-containing proteins,
60 such as the four and a half LIM domain protein 2 (FHL-2), to β integrin chains⁴⁰. In addition, a point
61 mutation in the β 1 integrin tail, which mimics the high-affinity talin-binding site naturally present in
62 the alternatively spliced β 1D integrin, negatively affected the localization of paxillin to adhesions⁴¹,
63 proposing that paxillin recruitment is also directly controlled by the β integrin peptide. This report is
64 consistent with data demonstrating a direct role for the Tyr⁷⁴⁷ residue, located in the membrane-
65 proximal talin-binding NPLY⁷⁴⁷ motif, in controlling paxillin localization to β 3 integrin complexes
66^{42,43}. Interestingly, modifications of this sequence or nearby residues, affected paxillin binding to
67 adhesions^{43,44}. Importantly, even in the presence of functional integrin/talin complexes that induced
68 integrin activation and clustering, paxillin recruitment still required their mechanical linkage to the
69 actin cytoskeleton^{45,46}. Remarkably, paxillin displayed a mechanosensitive behavior on stress fibers
70³⁴ and could bind detergent extracted and stretched cytoskeletons, proposing the existence of tension-
71 induced paxillin-binding sites³⁰. Combined with the notion that some LIM domains can bind Tyr-
72 containing peptide motifs^{47,48} similar to the NPLY sequence of β 3 integrin, we previously
73 hypothesized that paxillin LIM domains recognize the β 3 integrin Y⁷⁴⁷-presenting motif in a tension-
74 dependent manner⁴².

75 While the central role of paxillin in the signal transduction from the integrin/talin/kindlin complex is
76 well accepted, it is still controversial how it interacts with these proteins and whether it directly binds
77 β integrin subunits^{21,49,50}. Aiming for a better understanding of the integrin-dependent mechanisms
78 of paxillin recruitment to FAs, we studied the previously reported paxillin-binding defective β 3^{VE/YA}
79 integrin in more detail⁴³. This integrin, which contains the VE high-affinity talin-binding motif from
80 layilin combined with the Y⁷⁴⁷A mutation, affected β 3 integrin-dependent spreading on vitronectin
81 and reduced the recruitment of endogenous paxillin to FAs⁴³. Here we show that β 3^{VE/YA} integrin-
82 containing adhesions exhibit remarkable defects of stability, despite almost normal dissociation
83 dynamics of talin and β 3 integrin. The mechanical coupling of paxillin to such an integrin or the
84 plasma membrane, rescued the FA instability, highlighting a critical role of paxillin in the mechanical
85 stabilization of the integrin/talin linkage. Importantly, LIM domains appeared sufficient for this
86 rescue, suggesting that they are critical structural components of FAs. By elucidating the mechanisms
87 of LIM domain-mediated paxillin recruitment to β 3 integrin-containing adhesions, we revealed a
88 defined spatial orientation of paxillin LIM domains, in which LIM4 interacts with the plasma
89 membrane. We also demonstrated that upon deletion of LIM3, the strong paxillin recruitment defect
90 is caused by a steric misplacement of LIM1 and LIM2, forming a major FA-binding element. This

91 proposes a new model in which a defined spacing of the LIM domains, as well as their correct
92 positioning, is critical for reading the presence of mechanical tension occurring in the
93 integrin/talin/kindlin/F-actin linkage.

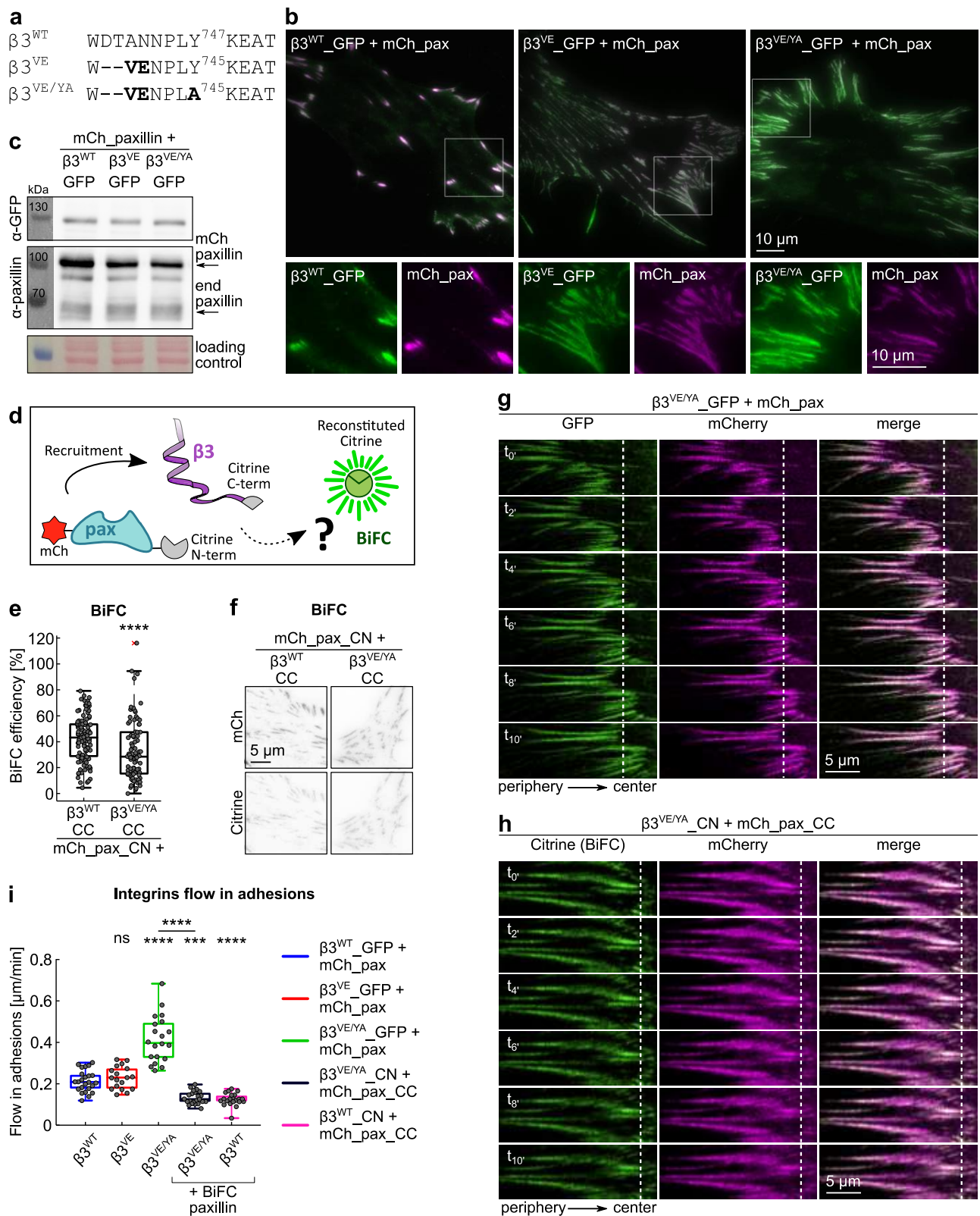
94 **Results**

95 **Paxillin anchoring to signaling-defective integrins rescues a rapid-sliding adhesion** 96 **phenotype**

97 To better understand the mechanism of paxillin recruitment to $\beta 3$ integrin-containing focal adhesions,
98 we employed the previously reported $\beta 3$ integrin mutants, $\beta 3^{VE}$ and $\beta 3^{VE/YA}$ (Fig. 1a), known to
99 modulate the binding of talin, and potentially disrupting the paxillin binding site⁴³. While the first
100 mutant presents the high-affinity talin-binding motif (VE), the second, additionally contains the
101 Y⁷⁴⁵A mutation, which created a spreading-incompetent and paxillin-recruitment deficient integrin
102 ⁴³. Nevertheless, prolonged culturing of $\beta 3^{VE/YA}$ integrin-expressing NIH-3T3 fibroblasts in the
103 presence of serum allowed spreading, FA assembly and their phenotypic analysis (Fig. 1b). Prominent
104 GFP-positive central adhesions were induced by the high-affinity talin-binding motif ($\beta 3^{VE}$), but
105 lacking in the $\beta 3^{VE/YA}$ integrin-expressing cells (Fig. 1b). At the same time, the latter cells presented
106 much thinner and more elongated FAs (Fig. 1b). Moreover, live cell imaging of $\beta 3^{VE/YA}$ integrin-
107 expressing cells unveiled a striking FA instability and accelerated retrograde sliding, when compared
108 to $\beta 3^{WT}$ and $\beta 3^{VE}$ integrin-containing adhesions (Supplementary Movies 1 and 2). Importantly, this
109 differential FA stability was not linked to altered expression levels of transfected proteins (Fig. 1c).
110 Considering the previously reported diminished recruitment of paxillin to $\beta 3^{VE/YA}$ integrin, the
111 enhanced apparent sliding of FAs presenting this receptor was intriguing. In fact, it contradicted
112 current models proposing that an increased paxillin recruitment is associated with enhanced adhesion
113 turnover^{8,51}. We therefore assessed paxillin recruitment to $\beta 3^{VE/YA}$ -adhesions and determine whether
114 this fulfils a critical role in activating the clutch between the substrate-bound integrin and the
115 retrogradely moving F-actin network⁴.

116 Bimolecular Fluorescence Complementation (BiFC) was used as a tool to measure paxillin
117 recruitment to $\beta 3$ integrin-positive adhesions in living cells. Accordingly, mCherry_paxillin and
118 $\beta 3^{WT}/\beta 3^{VE/YA}$ integrins C-terminally tagged with complementary citrine fragments were co-
119 expressed, as shown in Fig. 1d. Transfected NIH-3T3 cells, recognized in virtue of their mCherry
120 emission, were imaged *via* TIRF microscopy, in order to detect the BiFC-derived citrine fluorescence.
121 Although both combinations of proteins generated BiFC (Fig. 1e,f and Supplementary Fig 1a), the
122 VE/YA mutation significantly reduced the efficiency, confirming a diminished recruitment of paxillin

123 to $\beta 3^{VE/YA}$ integrin⁴³. However, the generation of BiFC proposed that exogenously expressed paxillin
124 could be transiently recruited to $\beta 3^{VE/YA}$ -FAs, potentially relying on endogenous integrins, or
125 interactions with other FA-proteins such as kindlin or talin^{16,36-38,43}. Nevertheless, the reduced BiFC
126 efficiency could result from an impaired and very transient paxillin binding to $\beta 3^{VE/YA}$ -containing
127 adhesions, which reduced the complementation of the citrine fragments⁵²⁻⁵⁴. Strikingly, the
128 establishment of a BiFC-based mechanical coupling of paxillin to $\beta 3^{VE/YA}$ integrin rescued the FA
129 sliding phenotype (Fig. 1g-h and Supplementary Movie 3). These observations were confirmed by
130 the quantification of the flow of the integrin-associated fluorescence in a frame-by-frame pixel-flux-
131 based algorithm (Fig. 1i and Supplementary Fig. 1b). Indeed, the VE/YA mutation almost doubled
132 the apparent displacement of integrins per minute ($\beta 3^{WT}$ 0.21 $\mu\text{m}/\text{min}$, $\beta 3^{VE/YA}$ 0.40 $\mu\text{m}/\text{min}$), but,
133 after the BiFC-based trapping of paxillin, the stability was recovered ($\beta 3^{VE/YA}$ + BiFC 0.13 $\mu\text{m}/\text{min}$)
134 and even improved compared to $\beta 3^{WT}$ integrin-containing adhesions. Interestingly, in the presence of
135 the mechanical integrin-paxillin coupling, the displacements of $\beta 3^{WT}$ and $\beta 3^{VE/YA}$ containing FAs
136 were indistinguishable (Fig. 1i). These results propose that the fast retrograde-sliding adhesion
137 phenotype induced by the $\beta 3^{VE/YA}$ integrin mutant was linked to a compromised paxillin binding and
138 retention within FAs, possibly impairing the maturation of highly dynamic integrin/talin clusters into
139 mature FAs⁴⁵.



140

141 **Figure 1 – Morphology and dynamics of wild-type and mutant $\beta 3_GFP$ integrin-positive**
 142 **adhesions.** (a) Sequence alignment of $\beta 3$ integrins, wt and mutants, at the NPLY⁷⁴⁷ motif. The high-
 143 affinity talin-binding chimeric $\beta 3$ integrins were obtained by introducing the VE motif from layilin.
 144 Bold indicates mutated residues. (b,c) NIH-3T3 cells transiently transfected with $\beta 3_GFP$ integrins,
 145 wild-type or mutants, and mCherry_paxillin. (b) Representative TIRF images of cells fixed 24 hours
 146 after spreading on glass coverslips in serum containing medium and (c) recombinant protein
 147 expression assessed by western blotting against GFP and total paxillin. Loading control: Ponceau

148 staining. **(d)** Schematic representation of the BiFC assay used to evaluate paxillin recruitment to $\beta 3$
149 integrins. **(e,f)** BiFC upon co-expression of mCherry_paxillin_CN and $\beta 3^{\text{WT}}_{\text{CC}}$ or $\beta 3^{\text{VE/YA}}_{\text{CC}}$ in
150 NIH-3T3 fibroblasts. **(e)** Quantification of the BiFC efficiency. Statistical analysis is provided in
151 Supplementary Table 1. **(f)** Representative TIRF images. **(g,h)** Kymographs representative of the
152 displacement of $\beta 3^{\text{VE/YA}}$ -containing adhesions, over a time period of 10 minutes, in the absence **(g)**
153 and in the presence **(h)** of mechanically (BiFC) coupled paxillin. **(i)** Quantification of the $\beta 3$ integrins
154 flow in adhesions, expressed as mean displacement over time ($\mu\text{m}/\text{min}$) per replicate. Statistical
155 analysis is provided in Supplementary Table 2.

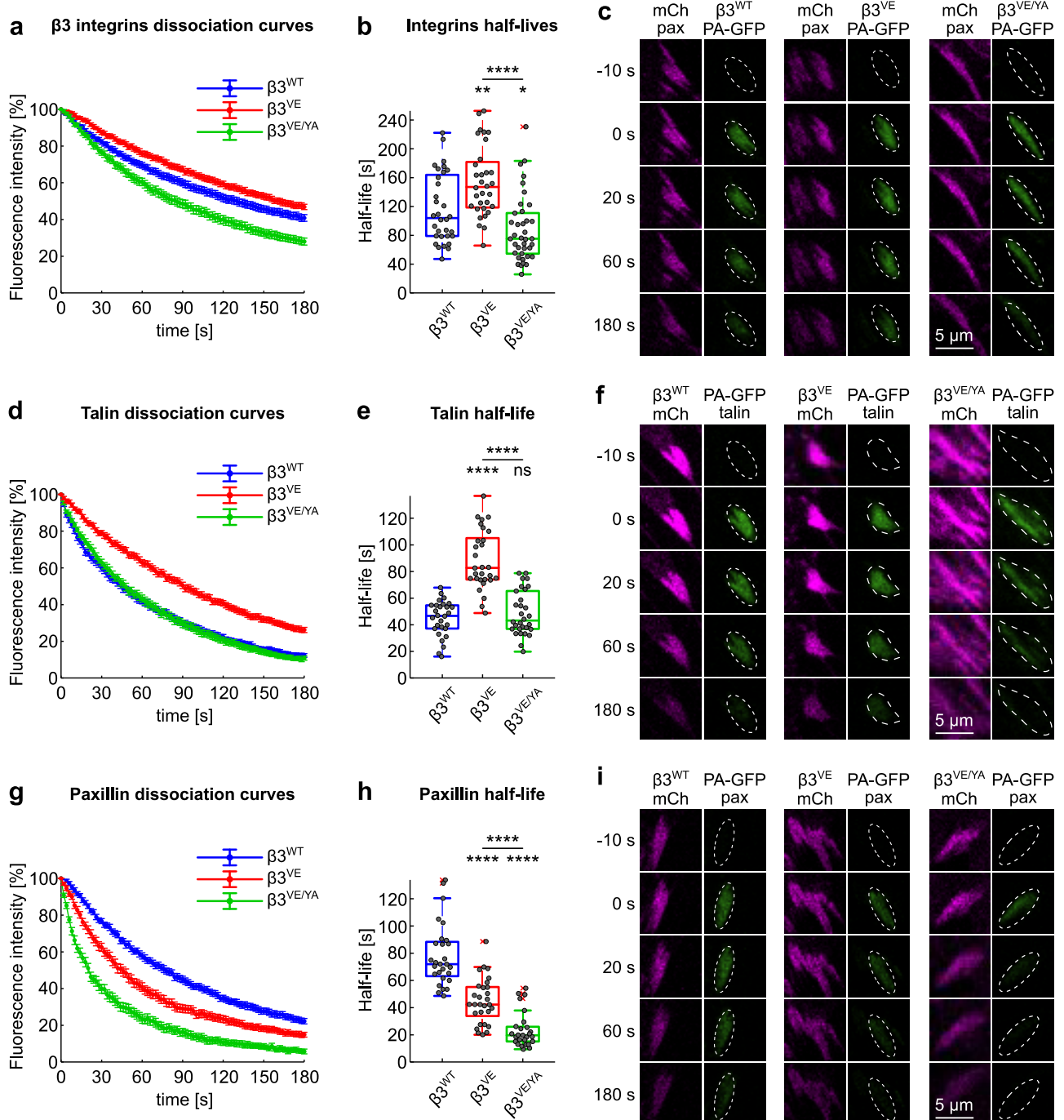
156 **Photoactivation of paxillin reveals its rapid dissociation from $\beta 3^{\text{VE/YA}}$ integrin-** 157 **containing adhesions**

158 Following the hypothesis that impaired paxillin binding caused the instability of $\beta 3^{\text{VE/YA}}$ -positive
159 FAs, paxillin dynamics at adhesion sites were investigated. Its dissociation rate was quantified *via*
160 photoactivation experiments, and used as a readout of its FA-binding capacity. Given the plausible
161 influence of the VE and VE/YA mutations on the dynamics of talin, and therefore of $\beta 3$ integrin itself
162 ⁴⁵, we first studied talin and integrin turnovers in their presence. To do so, $\beta 3$ integrins were C-
163 terminally tagged with the photoactivatable-GFP (PA-GFP), co-expressed with mCherry_paxillin and
164 photoactivated in a single mCherry-positive peripheral FA. The fluorescence loss after
165 photoactivation demonstrated that the high-affinity talin-binding motif (VE) enhanced the stability of
166 the $\beta 3$ integrin, prolonging its half-life ($t_{1/2}$) in adhesions by 1.4-fold (median $t_{1/2}$ of $\beta 3^{\text{WT}}$ 104 sec *vs*
167 147.1 sec of $\beta 3^{\text{VE}}$ integrin). However, for the $\beta 3^{\text{VE/YA}}$ integrin mutant, the dissociation dynamics was
168 increased, and the median of the estimated half-lives was 75.3 sec, meaning 0.75-fold that of the wild-
169 type integrin (Fig. 2a-c and Supplementary Fig. 3d).

170 To measure the talin off-rate, a similar photoactivation strategy was applied, with the $\beta 3$ integrin
171 carrying the mCherry tag. Coherent with the slower turnover of the $\beta 3^{\text{VE}}$ integrin, the half-life of PA-
172 GFP_talin was prolonged in $\beta 3^{\text{VE}}$ - compared to $\beta 3^{\text{WT}}$ -positive adhesions (82.6 sec and 46.7 sec,
173 respectively). Talin dissociation from $\beta 3^{\text{VE/YA}}$ integrin-adhesions (43.2 sec) was instead almost
174 identical to that observed with the wild-type receptor (Fig. 2d-f and Supplementary Fig. 3e).
175 Nevertheless, the ratio between half-lives, revealed a stabilization of talin on the VE-expressing
176 integrins: the half-life of talin in respect to that of wild-type $\beta 3$ integrin was 0.4, while increased to
177 0.6 in FAs containing $\beta 3^{\text{VE}}$ or $\beta 3^{\text{VE/YA}}$ integrins.

178 Considering the intricate network of paxillin interactions, we assured that the tagging of paxillin did
179 not affect its binding capacity to FA-complexes. The equivalent dissociation rate of recombinant
180 paxillins, presenting the PA-GFP either at the N- or C-terminus, indicated that the fusion of tags at
181 the extremities did not alter its binding FAs (Supplementary Fig. 3a-c). Surprisingly, the VE motif,
182 which increased the affinity of talin for the $\beta 3$ tail by about 20-fold ⁴³ and reduced the dissociation

183 rate of these two proteins from FAs, caused a faster dissociation of paxillin and a shortening of its
 184 half-life by approximately 40% (paxillin $t_{1/2}$ in $\beta 3^{WT}$ adhesions 72 sec, while in $\beta 3^{VE}$ adhesions 42.3
 185 sec) (Fig. 2g-i and Supplementary Fig. 3f). Adding the Y⁷⁴⁷A substitution into the $\beta 3^{VE}$ integrin
 186 sequence further destabilized paxillin binding to FAs and shortened its half-life to less than 30% (19.7
 187 sec) (Fig. 2g-i and Supplementary Fig. 3f). Therefore, the impact of the VE/YA mutation was much
 188 greater on the dynamics of paxillin than on talin (almost unaltered between $\beta 3^{VE/YA}$ and $\beta 3^{WT}$
 189 adhesions) and $\beta 3$ integrin ($t_{1/2}$ of $\beta 3^{VE/YA}$ reduced of 25% compared to that of $\beta 3^{WT}$). Importantly,
 190 these dynamic measures of paxillin dissociation would propose a highly compromised paxillin
 191 binding to $\beta 3^{VE/YA}$ adhesions, which might be functionally linked to their rapid-sliding phenotype.

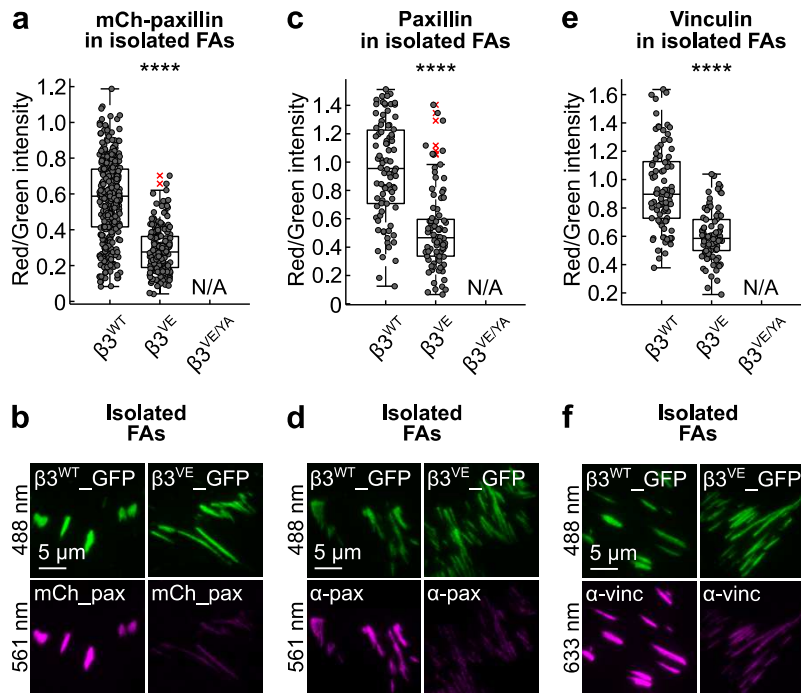


193 **Figure 2 – Analysis of the dissociation dynamics of the $\beta 3$ integrin/talin/paxillin complex. (a,d,g)**
194 Experimental dissociation curves of (a) $\beta 3$ _PA-GFP integrins from mCherry_paxillin-positive focal
195 adhesions and of (d) PA-GFP_talin and (g) PA-GFP_paxillin from $\beta 3$ _mCherry-positive focal
196 adhesions. (b,e,h) Box plot of the half-lives of (b) $\beta 3$ _PA-GFP integrins in mCherry_paxillin-positive
197 FAs and of (e) PA-GFP_talin and (h) PA-GFP_paxillin in $\beta 3$ _mCherry-positive FAs. Statistical
198 analysis is provided in Supplementary Table 3. (c,f,i) Representative images of photoactivation time
199 series of experiments in a-b, d-e and f-g.

200 **Paxillin dissociation dynamics reflects the mechanical stability of isolated focal** 201 **adhesions**

202 Since the rapid inward-sliding of $\beta 3^{VE/YA}$ integrin-presenting FAs was potentially linked to the fast
203 dissociation of paxillin from them, it appeared relevant to characterize the mechanical stability of the
204 entire FA-complex with an alternative approach. We therefore applied the protocol developed by Kuo
205 *et al.* to isolate apparently intact FAs, and we revealed their mechanical integrity in respect to the
206 expressed GFP-tagged $\beta 3$ integrin construct. Consistent with the rapid displacement of $\beta 3^{VE/YA}$
207 integrin-containing adhesions, these apparently mechanical fragile structures, did not survive the FA-
208 isolation procedure. On the contrary, the shearing of the PM, the washing away of the cytosol with a
209 jet of PBS⁵⁵ and the subsequent fixation, allowed detecting isolated FAs containing $\beta 3^{WT}$ or $\beta 3^{VE}$
210 integrins in virtue of their fluorescence (Fig. 3a,b). Importantly, these isolated adhesive structures
211 were mCherry_paxillin-positive. Reasonably, the dissociation curves of the photoactivation studies
212 reflected the strength of paxillin binding to FAs, which determined its ability to remain associated
213 during the FA-isolation process. Indeed, while in intact cells, paxillin was recruited to $\beta 3^{WT}$ and $\beta 3^{VE}$
214 adhesions equally well (Fig. 1b), in isolated FAs, the expression of the $\beta 3^{VE}$ integrin variant caused
215 a drop of paxillin/integrin fluorescence ratio of about 50% (Fig. 3a,b), which was consistent with the
216 accelerated dissociation rate of paxillin from this type of adhesions (Fig. 2g,h). To assure that the
217 mCherry-tag and the exogenous paxillin expression did not affect its mechanical retention in FAs,
218 cells were transfected only with the integrin proteins and the presence of endogenous paxillin in
219 isolated adhesions was verified by immunostaining. As for the mCherry-labelled paxillin, the
220 immunofluorescence signal dropped in adhesions presenting the $\beta 3^{VE}$, compared to the wild-type
221 integrin (Fig. 3c,d). We also evaluated the binding of vinculin and demonstrated its reduction in $\beta 3^{VE}$
222 integrin-containing, compared to $\beta 3^{WT}$ integrin-, adhesions (Fig. 3e,f). This was unexpected
223 considering the proposed talin-dependent recruitment and binding of vinculin to adhesions and the
224 expression of an integrin with a high-affinity talin-binding site^{2,4,39,43}. However, it was consistent
225 with a critical role of paxillin in orchestrating the nanoscale localization of vinculin within FAs¹⁰.
226 Accordingly, it has been demonstrated that paxillin and vinculin have comparable recovery curves
227 after photobleaching⁵⁶, proposing that the VE mutation loosened vinculin binding to FAs, in a
228 paxillin-dependent manner. These results suggested that, despite a high-affinity talin/integrin

229 interaction, a proper paxillin-mediated focal adhesion assembly and maturation is required to firmly
 230 anchor cells to the substratum and to create FAs with sufficient mechanical cohesion to survive the
 231 isolation protocol.



232

233 **Figure 3 – Analysis of paxillin and vinculin binding upon isolation of FA-complexes. (a,c,e)**
 234 Quantification of cytoplasmic proteins retained in $\beta 3^{\text{WT}}$ _GFP- or $\beta 3^{\text{VE}}$ _GFP-positive FAs, isolated
 235 from NIH-3T3 fibroblasts. (a) mCherry_paxillin, (c) endogenous paxillin and (e) endogenous
 236 vinculin. Statistical analysis is provided in Supplementary Table 4. (b,d,f) Representative TIRF
 237 images of FAs isolated from NIH-3T3 cells of experiments quantified in a, c and e.

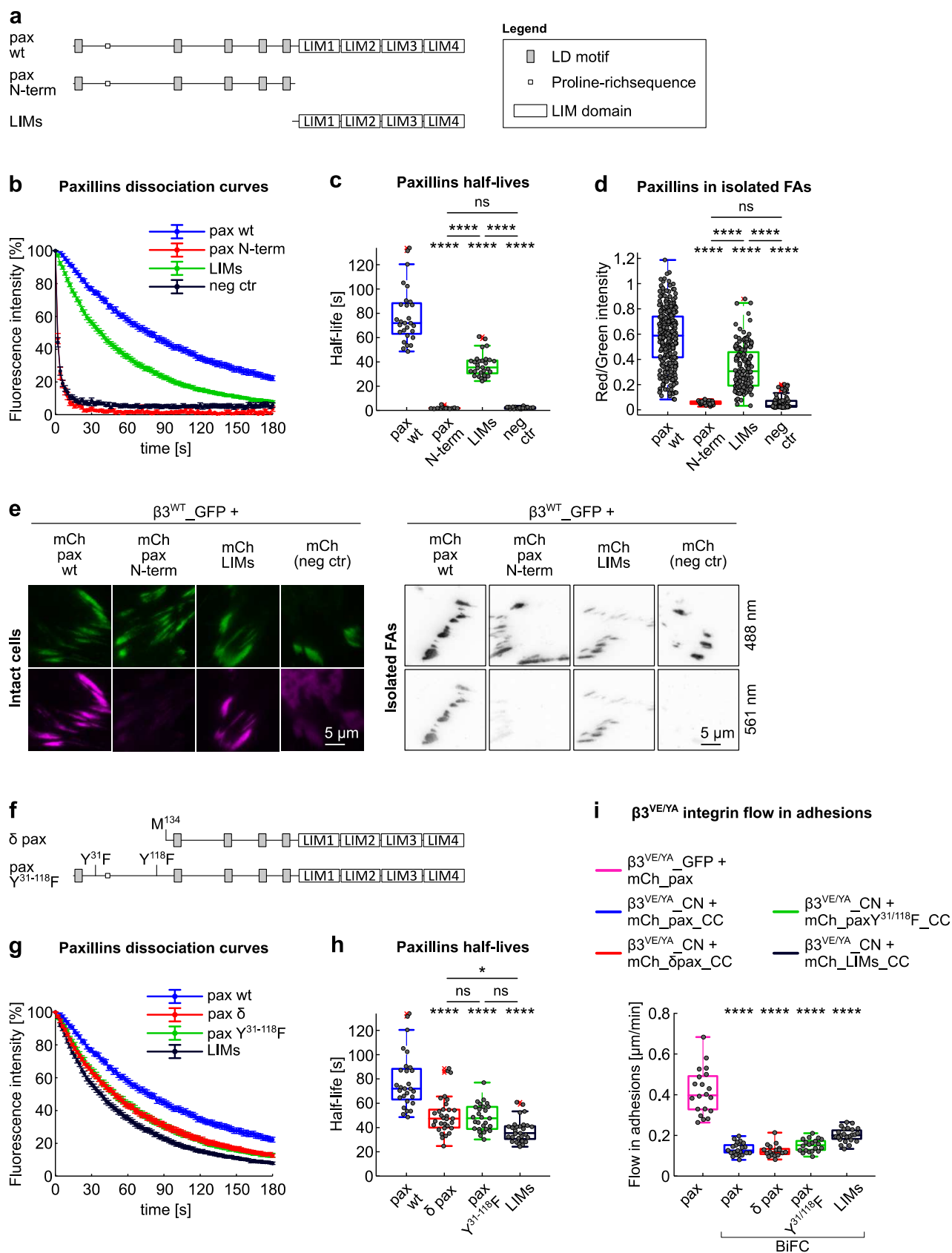
238 **The N-terminal, LD motif-containing sequence, enhances paxillin stability in FAs**

239 By applying photoactivation and FA-extraction protocols to two paxillin fragments corresponding to
 240 the N-terminal LD motif-containing sequence and to the C-terminal LIM domains respectively (Fig.
 241 4a), we confirmed the previously proposed FA-targeting activity of the second²¹. Although the N-
 242 terminal paxillin fragment could be photoactivated and detected in the area corresponding to FAs
 243 (Supplementary Fig. 2a), it showed no specific retention and dissociated similarly to the
 244 cytoplasmically located PA-GFP control (median half-life of 1.8 and 2 sec, respectively) (Fig. 4b,c
 245 and Supplementary Fig. 3g). Accordingly, this paxillin fragment was not detected in isolated
 246 adhesions above control levels (Fig. 4d,e). In contrast, the LIM domain-only construct (paxillin C-
 247 terminus) was efficiently photoactivated (Supplementary Fig. 2a), retained in FAs for a prolonged
 248 period ($t_{1/2}$ about 50% of full-length paxillin) (Fig. 4b,c and Supplementary 3g) and significantly
 249 present in isolated FAs (Fig. 4d,e). Despite the evident interaction of the paxillin LIM domain-only
 250 protein with FAs, our analyses revealed that it dissociated significantly faster than the full-length

251 paxillin, and was less retained in isolated FAs (LIMs/integrin fluorescence 59% in respect to
252 paxillin/integrin). These data, therefore, support an auxiliary function of paxillin N-terminal
253 sequences in stabilizing the LIM domain-dependent localization at FAs.

254 To circumscribe this stabilization activity to a specific paxillin sequence, the dynamic behavior of δ
255 paxillin, a naturally occurring paxillin isoform missing the first 133 amino acids (Fig. 4f), was
256 investigated. Compared to LIMs-only, δ paxillin showed an improved stability (median $t_{1/2}$ 35.4 sec
257 and 47.4 sec, respectively), but still a dissociation rate significantly faster than that of the canonical
258 paxillin (72 sec), proposing the presence of important residues within the missing amino acids (Fig.
259 4g,h and Supplementary Fig. 2b and 3h). Interestingly, δ paxillin lacks tyrosines 31 and 118, which
260 phosphorylation enhances FAK and vinculin binding^{10,14,57}. When their phosphorylation was
261 prevented by means of site-directed mutagenesis (paxillin Y^{31/118}F, Fig. 4f), the resulting dissociation
262 curve overlaid that of δ paxillin. These results are consistent with the hypothesis that paxillin
263 stabilization in adhesion occurs in response to phosphorylation of the Y³¹ and/or Y¹¹⁸, potentially
264 leading to an exposure of LD motifs that enables a mechanical interaction with other components of
265 FAs, such as talin, FAK, and vinculin^{10,16,21,58,59}.

266 Considering this novel stabilizer function of the paxillin N-terminus, we tested if the paxillin-
267 dependent arrest of $\beta 3^{\text{VE/YA}}$ integrin-positive FAs relied on its activity. Although the BiFC-based
268 mechanical coupling of δ paxillin or paxillin Y^{31/118}F to the mutant integrin was as efficient as the
269 wild-type protein, the LIM domains alone were, surprisingly, sufficient to arrest the inward flow of
270 $\beta 3^{\text{VE/YA}}$ integrin in adhesion to wild-type levels ($\beta 3^{\text{VE/YA}}$ + LIMs BiFC 0.20 $\mu\text{m}/\text{min}$, $\beta 3^{\text{WT}}$ without
271 BiFC 0.21 $\mu\text{m}/\text{min}$) (Fig. 4i). This further corroborated a critical function of the LIM domains in
272 mechanically stabilizing integrin/talin complexes, thus suggests an essential structural role of paxillin
273 in FAs.



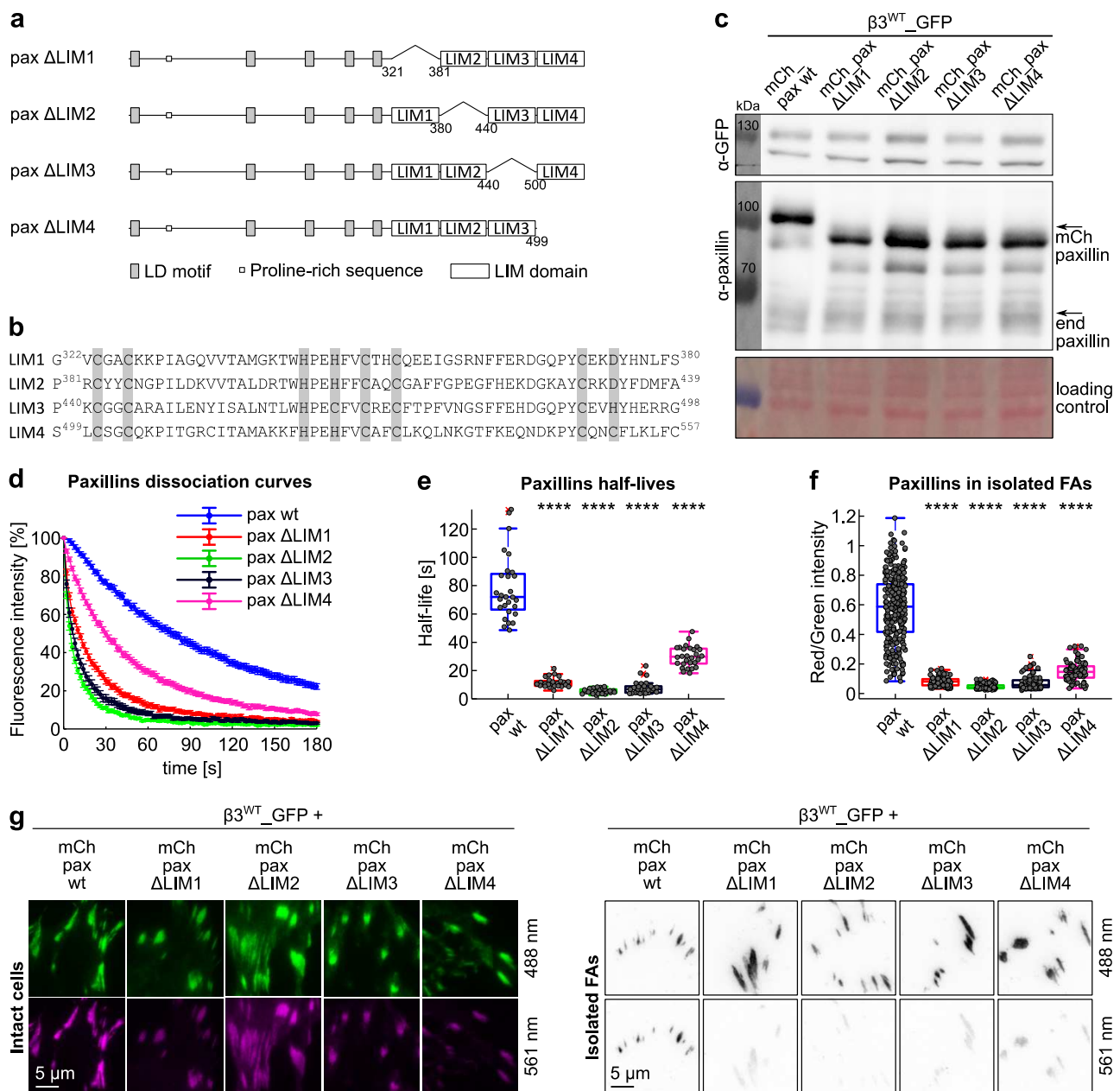
274

275 **Figure 4 – Paxillin binding to adhesions is driven by the LIM domains but stabilized by the N-**
 276 **terminus.** (a,f) Schematic representation of paxillin (a) truncation mutants and (f) N-terminal
 277 mutants. All proteins were N-terminally tagged with PA-GFP or mCherry. (b,g) Experimental
 278 dissociation curves of PA-GFP_paxillin wt and (b) truncation mutants or (g) N-terminal mutants,
 279 from β_3 _mCherry-positive FAs. (c,h) Box plot of the half-life of PA-GFP_paxillin wt and (c)

280 truncation mutants or **(h)** N-terminal mutants, in $\beta 3$ _mCherry-positive FAs. Statistical analysis is
281 provided in Supplementary Table 3. **(d)** Quantification of mCherry_paxillin wt and truncation
282 mutants retained in FAs, isolated from NIH-3T3 cells co-expressing $\beta 3^{\text{WT}}$ _GFP. Statistical analysis
283 is provided in Supplementary Table 4. **(e)** Representative TIRF images of FAs in NIH-3T3 cells co-
284 expressing $\beta 3^{\text{WT}}$ _GFP and mCherry_paxillin proteins. Left panel: FAs in intact cells; right panel:
285 isolated FAs. **(i)** Quantification of the $\beta 3^{\text{VE/YA}}$ integrin flow in adhesions, expressed as mean
286 displacement over time ($\mu\text{m}/\text{min}$) per replicate. Statistical analysis is provided in Supplementary
287 Table 2. Neg ctr: PA-GFP in photoactivation experiments and mCherry in isolated FAs.

288 **Differential contribution of LIM domains to paxillin docking to FAs**

289 To precisely assess the contribution of each LIM domain to paxillin docking to FAs, we designed
290 paxillin mutants missing individual LIM domains (Fig. 5a,b and Supplementary Fig. 4a), verified
291 their proper expression (Fig. 5c), and analyzed them by photoactivation and FA-isolation
292 experiments. This first approach unveiled a wide range of paxillin dissociation dynamics (Fig. 5d,e
293 and Supplementary Fig. 2c and 3i), strongly correlating with the quantitative analysis of mechanical
294 retention in isolated FAs (Fig. 5f,g). Specifically, the medians of the dissociation half-lives measured
295 for paxillin- ΔLIM1 , - ΔLIM2 , - ΔLIM3 and - ΔLIM4 were respectively 15%, 7%, 9% and 42% of that
296 of paxillin wt (Fig. 5e). Similarly, the residual normalized paxillin-derived fluorescence in isolated
297 adhesions was 14%, 7%, 10% and 25% compared to that of mCherry_paxillin wt (Fig. 5f). In line
298 with previous qualitative observations^{21,35}, the deletion of LIM4 was significantly the least severe,
299 while surprisingly the LIM1 and LIM2 deletions were comparable to that of LIM3, which so far
300 represented the most critical FA-interaction domain. These results suggested the existence of multiple
301 FA-interaction sites, spread along the four LIM domains. Except for LIM4, which removal would not
302 affect the spacing between LIM1-LIM2-LIM3 domains, the outcome of all other LIM-deletions could
303 also reflect the mis-localization of the remaining LIM domains, preventing to identify the specific
304 binding function of the missing LIM domain.



305

306 **Figure 5 – LIM domain deletion analysis by photoactivation and FA-isolation.** (a) Schematic
 307 representation of the paxillin LIM domain deletion mutants. All proteins were N-terminally tagged
 308 with PA-GFP or mCherry. (b) Alignment of the four paxillin LIM domains. Grey: zinc-binding
 309 residues. (c) Western blot of protein extracts from NIH-3T3 fibroblasts transiently co-expressing
 310 $\beta^{\text{WT}}_{\text{GFP}}$ and mCherry-tagged paxillin proteins, wt or deletion mutants. Loading control: Ponceau
 311 staining. (d) Experimental dissociation curves of PA-GFP_paxillin wt and deletion mutants from
 312 $\beta^{\text{WT}}_{\text{mCherry}}$ -positive FAs. (e) Box plot of the corresponding half-lives. Statistical analysis is
 313 provided in Supplementary Table 3. (f) Quantification of mCherry_paxillin wt and mutants retained
 314 in FAs isolated from NIH-3T3 cells co-expressing $\beta^{\text{WT}}_{\text{GFP}}$. Statistical analysis is provided in
 315 Supplementary Table 4. (g) Representative TIRF images of FAs in NIH-3T3 cells co-expressing
 316 $\beta^{\text{WT}}_{\text{GFP}}$ and mCherry_paxillin proteins. Left panel: FAs in intact cells; right panel: isolated FAs.

317 **LIM domains are not interchangeable and LIM2 is the major determinant of paxillin**
318 **docking to FAs**

319 Because of the confounding factor generated by the LIM domain deletion strategy, which abolished
320 the function of a LIM domain but at the same time also destroyed their respective spacing (with the
321 exception of LIM4 truncation), we developed the *LIM domain replacement strategy* (Fig. 6a and
322 Supplementary Fig. 4b).

323 A specific LIM1 domain-associated function was revealed by replacing it by either LIM2 or LIM3,
324 and assessing the FA-dissociation dynamics of the resulting paxillin 2234 and paxillin 3234 proteins
325 (Fig. 6b,c and Supplementary Fig. 2d and 3j). While both mutants partially rescued the deletion of
326 LIM1, none of them presented a level of FA-binding comparable to that of paxillin wt, indicating a
327 missing LIM1-dependent interaction. Nevertheless, LIM2 was slightly more efficient than LIM3 in
328 rescuing LIM1, proposing that despite the high degree of homology among their primary structure,
329 LIM2 presents some residues that better mimicked the precise and unique signature of LIM1.

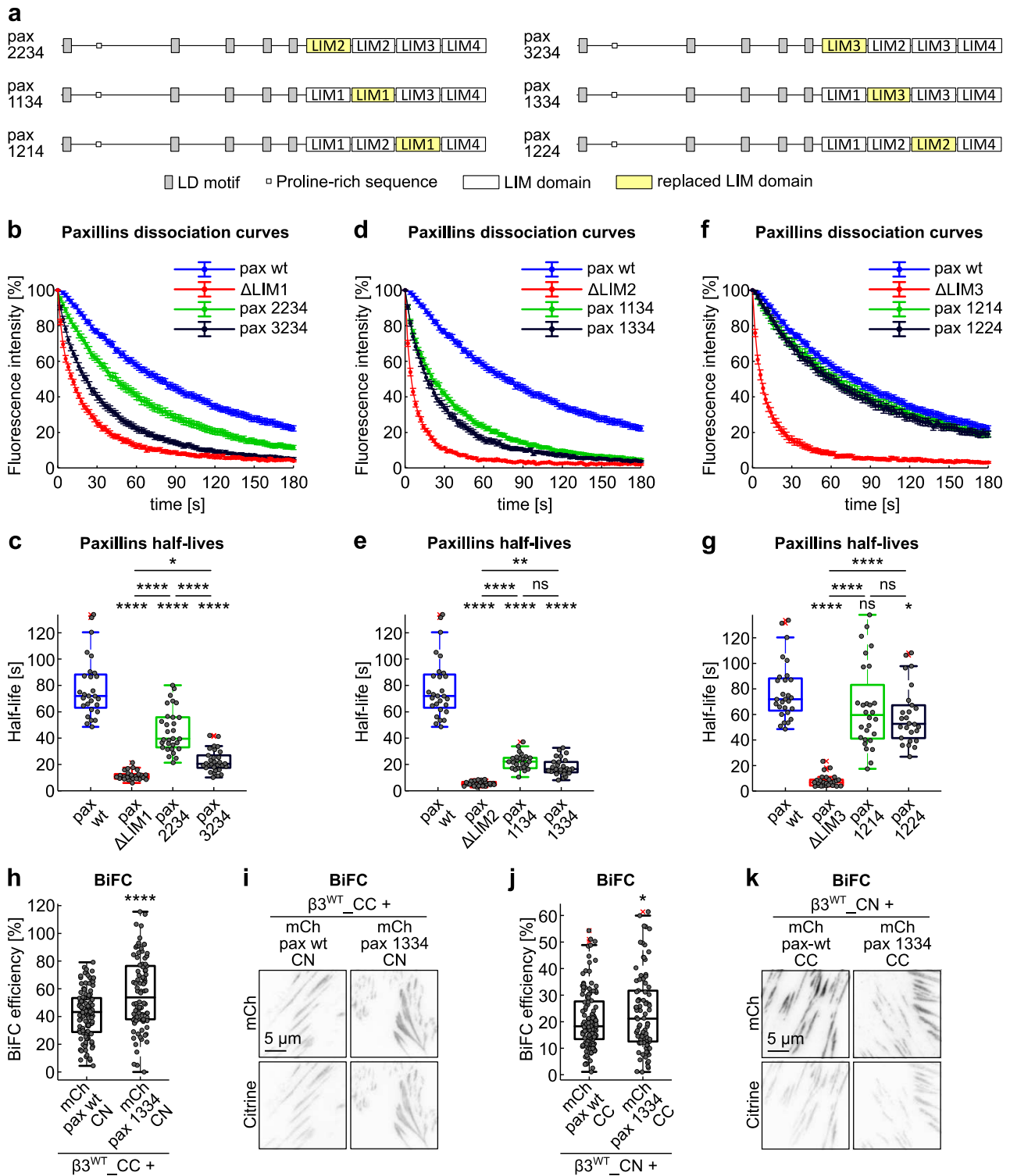
330 The half-life of paxillin lacking LIM2 (paxillin Δ LIM2, 5.1 sec) was only slightly improved by
331 duplicating LIM1 (paxillin 1134, 22.1 sec) or LIM3 (paxillin 1334, 16.4 sec) (Fig. 6d,e and
332 Supplementary Fig. 2d and 3k). These data favor the hypothesis that the LIM2 domain does possess
333 exclusive features and an irreplaceable function that none of the other structurally similar paxillin
334 LIM domains can execute.

335 When based on the sole analysis of the LIM domain deletion mutants, we would have expected that
336 LIM3 is carrying key determinants of paxillin binding to FAs, confirming the previously proposed
337 findings by Brown *et al.*²¹. However, the LIM3 replacement by either LIM1 or LIM2, caused no
338 significant (paxillin 1214) and only a minor (paxillin 1224) acceleration of paxillin dissociation from
339 FAs, when compared to the wild-type protein (Fig. 6f,g and Supplementary Fig. 2d and 3l). This
340 corresponds to an efficient rescuing of the LIM3 deletion and proposes that a LIM3 domain-specific
341 function is unlikely to be sequence-dependent, but rather relying on its overall 3D-folding, faithfully
342 reproduced by both LIM1 and LIM2. In fact, it raises the possibility that LIM3 has an important role
343 in creating the correct distance between LIM1-LIM2 and LIM4 domains, assuring their correct spatial
344 separation when binding to the FA-complex.

345 Finally, relying on a BiFC approach, we demonstrated that the paxillin binding to FAs, but not its
346 recruitment was altered by the LIM domain replacement strategy. Emblematic of these two distinct
347 phenomena is the analysis of paxillin 1334, which was among the least retained mutant (Fig. 6d,e),
348 showing a dissociation curve comparable to that of wild-type paxillin from $\beta 3^{VE/YA}$ integrin-
349 containing FAs (Fig. 2g,h), yet accomplishing a BiFC of $\beta 3^{WT}$ integrin at least as efficient as the wt

350 paxillin (Fig. 6h,i). Consistent BiFC results were obtained upon exchange of citrine fragments among
351 paxillin and integrin (Fig. 6j,k), confirming that the replacement of the LIM2 by LIM3 domain
352 resulted in a protein (paxillin 1334) unable to make stable interactions with FAs, which was however
353 well, but only transiently, recruited to these sites.

354 Overall, these data revealed that individual LIM domains have specific FA-interaction functions
355 linked to their respective position in the LIM domain repeats. Moreover, the efficient BiFC between
356 paxillin 1334 and the C-terminus of $\beta 3$ integrin suggests that despite reduced retention in FAs and
357 the absence of the pivotal LIM2 domain, the mechanisms of recruitment of the LIMs-array in respect
358 to the C-terminal end of the integrin tail was not altered.



359

360 **Figure 6 – LIM domain-specific functions assessed by the LIM domain replacement strategy.**
 361 (a) Schematic representation of the paxillin mutants obtained by the LIM domain replacement
 362 strategy. From the top line: replacement of LIM1, replacement of LIM2 and replacement of LIM3.
 363 All proteins were N-terminally tagged with PA-GFP. (b,d,f) Experimental dissociation curves of PA-
 364 GFP_paxillin wt and (b) LIM1 mutants, (d) LIM2 mutants and (f) LIM3 mutants, from $\beta 3$ _mCherry-
 365 positive FAs. (c,e,g) Box plot of the half-lives of PA-GFP_paxillin wt and (c) LIM1 mutants, (e)
 366 LIM2 mutants and (g) LIM3 mutants in $\beta 3$ _mCherry-positive FAs. Statistical analysis is provided in
 367 Supplementary Table 3. (h,i) BiFC upon co-expression of mCherry_paxillin_CN or its corresponding
 368 paxillin 1334 mutant and $\beta 3^{WT}$ integrin C-terminally tagged with the citrine C-terminal fragment in
 369 NIH-3T3 cells. (h) Quantification of the BiFC efficiency. Statistical analysis is provided in

370 Supplementary Table 1. (i) Representative TIRF images. (j,k) BiFC upon co-expression of
371 mCherry_paxillin_CC or its corresponding paxillin 1334 mutant and $\beta 3^{WT}$ integrin C-terminally
372 tagged with the citrine N-terminal fragment in NIH-3T3 cells. (j) Quantification of the BiFC
373 efficiency. Statistical analysis is provided in Supplementary Table 1. (k) Representative TIRF images.

374 **Paxillin LIM4 is a potential membrane binding and palmitoylated domain**

375 By sequence comparisons of the paxillin LIM domains, Beckerle and co-workers grouped the
376 homologous LIM1, LIM2 and LIM3 but classified differently LIM4²². When analyzed for specific
377 features, LIM4 stands out for its remarkably high positive charge (+5 compared to -1, -1 and -2 of
378 LIM1, LIM2 and LIM3 respectively). LIM4 is also unique for the presence of two conserved
379 cysteines that do not coordinate the binding of zinc atoms (Cys⁵¹² and Cys⁵⁵⁷-COOH) and remain
380 therefore potentially accessible for PTMs (Fig. 7a). Based on these peculiar and previously unnoticed
381 features we investigated a possible membrane binding function for the paxillin LIM4 domain,
382 intended to orient and stabilize paxillin in FAs. In fact, the cluster of basic residues could establish
383 nonspecific electrostatic interactions with acidic phospholipids of the PM while the abovementioned
384 cysteines can be *S*-acylated (i.e. palmitoylated), further strengthening this membrane association.

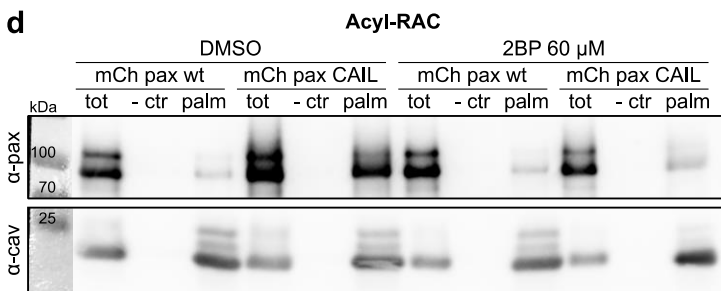
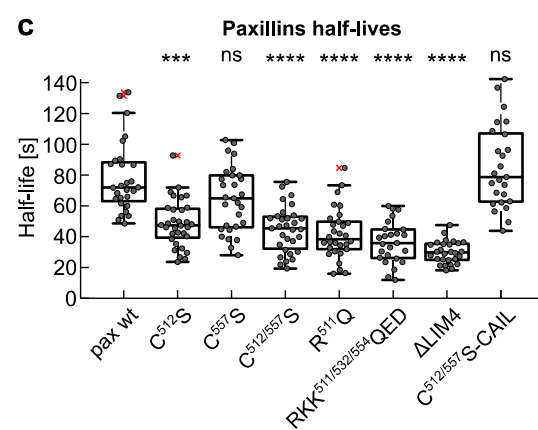
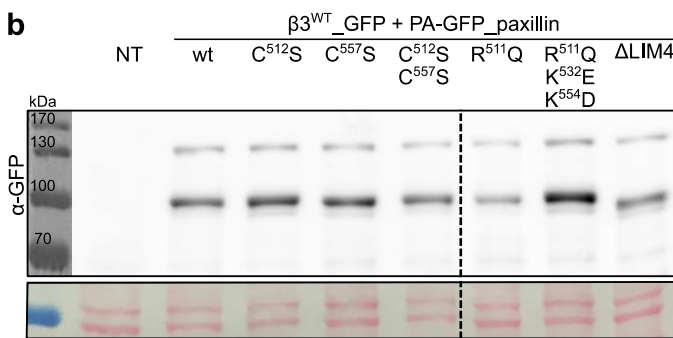
385 Considering the link between protein structure/function and selective pressure over evolution, an
386 alignment of paxillin LIM4 domain across species was performed (Fig. 7a). It appeared that this
387 domain is highly conserved, that the C-terminal cysteine, compared to C⁵¹², arose later during
388 evolution and that much simpler organisms, although containing several sequence modifications,
389 presented a perfectly intact GRC⁵¹² motif and an overall high net positive charge (Fig. 7a). As these
390 well-preserved features may be pivotal for the functioning of the domain, we sought to determine
391 their contribution to paxillin retention in FAs. Site-directed mutagenesis, preventing palmitoylation
392 at Cys^{512/557} or abrogating LIM4 positive charge, did not affect paxillin expression levels (Fig. 7b).
393 However, they reduced the half-life of paxillin in $\beta 3^{WT}$ integrin-positive FAs, as shown by
394 photoactivation experiments (Fig. 7c). Ensuring lipidation of the paxillin C^{512/557}S double mutant, by
395 adding to the paxillin C-terminus a CaaX-box (PA-GFP_paxillinC^{512/557}S-CAIL), rescued paxillin
396 FA-dissociation dynamics to wild-type levels (Fig. 7c). Interestingly, the mutation of the arginine
397 within the conserved GRC motif (R⁵¹¹Q) was comparable to the C⁵¹²S mutation (Fig. 7c), suggesting
398 that this residue (and G⁵¹⁰ as well) may function to allow the lipidation of the following cysteine. The
399 neutralization of paxillin LIM4 positive charge, by means of the RKK^{511/532/554}QED triple mutation,
400 reduced the retention of paxillin in FAs to the same extent as the deletion of the entire LIM4 domain
401 (Fig. 7c), demonstrating that its function relies on its positive charge, potentially orienting paxillin in
402 respect to the PM.

403 The Acyl-Resin Assisted Capture assay (Acyl-RAC), a valid tool to detect palmitoylated proteins
 404 among a total cell lysate, revealed a small but constant fraction of paxillin in the pool of palmitoylated
 405 proteins (Fig. 7d). The amount of palmitoylated paxillin strongly increased when, by means of the
 406 previously exploited CaaX-box (mCherry_paxillin-CAIL), an irreversible geranylgeranyl lipid anchor
 407 was coupled to the its carboxyl-terminus. Only in this context we appreciated the effect of the
 408 treatment with 2-bromopalmitate (2BP) that, competing with endogenous palmitate, acts as a general
 409 inhibitor of palmitate incorporation. Caveolin-1, because of its essentially irreversible palmitoylation
 410 ⁶⁰ is not sensitive to 2BP treatment and was therefore used as an internal positive control.

411 Overall, these data highlighted the relevance of LIM4 positive charges and demonstrated the
 412 palmitoylation of the paxillin protein, which is in line with a possible membrane binding function of
 413 the LIM4 domain.

a Conservation of the paxillin LIM4 domain across species

			net charge
<i>H. sapiens</i>	PXN	CSGCQK P ITG R CITAMAK K FH P E H FVCA F CL K QLNK G TF K E Q ND K PY C Q N C F L K LF C	+5
<i>R. norvegicus</i>	PXN	CSGCQK P ITG R CITAMAK K FH P E H FVCA F CL K QLNK G TF K E Q ND K PY C Q S C F L K LF C	+5
<i>M. musculus</i>	PXN	CSGCQK P ITG R CITAMAK K FH P E H FVCA F CL K QLNK G TF K E Q ND K PY C Q S C F V K LF C	+5
<i>G. gallus</i>	PXN	CSGCQK P ITG R CITAM G K K FH P E H FVCA F CL K QLNK G TF K E Q ND K PY C Q N C F L K LF C	+5
<i>X. laevis</i>	PXN	CSGCQK P ITG R CITAM G K K FH P E H FVCA F CL K QLNK G TF K E Q ND K PY C Q N C F V K LF C	+5
<i>D. rerio</i>	PXNA	CSGCQK P ITG R CITAM G K K FH P E H FVCA F CL K QLNK G TF K E Q ND K PY C Q S C F V K LF S	+5
<i>D. melanogaster</i>	Pax	CAG S K P ITG R CITAM F K K FH P E H FVCA F CL K QLNK G TF K E Q D K PY C H T C F D K I F G	+5
<i>C. elegans</i>	PXL1	CS Q C R G A I N G R C V A M G R K F H P E H F R S Y C N H Q L T K G T F K E V D R R R F C H K C Y N N T Y A L T P A	+6
<i>D. discoideum</i>	PAXB	CSGC G K A V S G R C V D A L D K K W H P E H F V C A F C M N P L A G G S Y T A N N G K P Y C K G C H N L F A	+3
LIM4 triple mutant		CSGCQK P ITG Q CITAMAK K FH P E H FVCA F CL E QLNK G TF K E Q ND K PY C Q N C F L D LF C	0



414
 415 **Figure 7 – Paxillin LIM4 domain carries membrane binding features relevant for FA binding.**
 416 (a) Alignment of the amino acid sequence of paxillin LIM4 across species and triple human paxillin
 417 LIM4 mutant (bottom). The latter was obtained by replacing three basic amino acids with neutral or

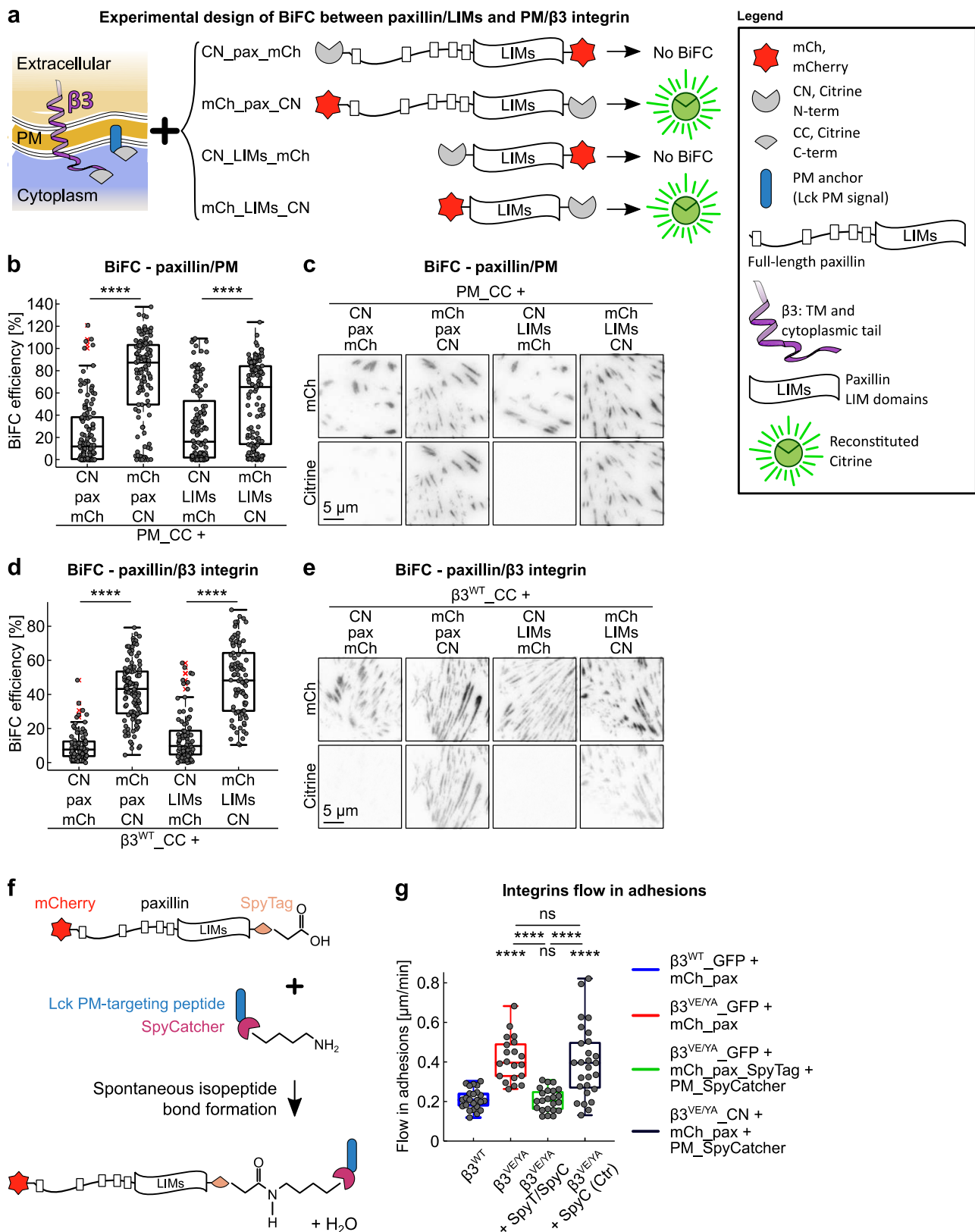
418 acidic residues found at the corresponding positions in other paxillin LIM domains
419 (RKK^{511/532/554}QED). Grey: zinc-binding residues; blue: positive residues; red: negative residues;
420 bold: non-conserved residues in respect to the human paxillin LIM4 domain; arrows indicate the
421 conserved free cysteines; yellow: conserved GRC motif. (b) Expression analysis, *via* western blot, of
422 the paxillin LIM4 mutants. Loading control: Ponceau staining. (c) Box plot of the half-lives of PA-
423 GFP_paxillin wt and LIM4 mutants in $\beta 3^{\text{WT}}$ _mCherry-positive FAs. Statistical analysis is provided
424 in Supplementary Table 3. (d) Acyl-Resin Assisted Capture assay from cell transiently transfected
425 with mCherry_paxillin wt or mCherry_paxillin-CAIL, untreated (DMSO) or treated with 2-
426 bromopalmitate. NT: not transfected; tot: total cell lysate; - ctr: negative control (tris-base); palm:
427 fraction of palmitoylated proteins (hydroxylamine); 2BP: 2-bromopalmitate.

428 **BiFC shows a defined spatial orientation of paxillin LIM domains within focal adhesions**

429 A possible function of a membrane-binding activity of LIM4, is to specifically orient the entire LIM
430 domain-array within FAs. Previous iPALM studies revealed a close membrane association of both
431 paxillin termini ⁶¹. However, based on various structures of two tandemly-organized LIM domains
432 (e.g. PDB ID: 1RUT and PDB ID: 2DFY), it is conceivable that the paxillin LIM1-LIM2-LIM3-
433 LIM4 array has an extended conformation. Because the BiFC efficiency is imposed by the relative
434 position of the proteins under analysis, as well as by the spatial orientation of the complementary
435 fluorophore fragments, we attempted to reveal the orientation of paxillin in respect to the PM by
436 BiFC. Accordingly, as summarized in Fig. 8a, differentially tagged recombinant paxillins were tested
437 for their ability to complement, in the context of $\beta 3$ -expressing fibroblasts (Swiss-3T3 ⁴³), a
438 membrane-anchored citrine fragment so localized *via* the PM-targeting peptide of Lck ⁶². Despite the
439 flexible nature of the paxillin amino-terminal half ⁶³, only the paxillin C-terminus appeared close
440 enough to the lipid bilayer for efficient BiFC with the PM-residing complementary probe (Fig. 8b,c).
441 Importantly, the spatial orientation of paxillin was encoded by the LIM domains, which yielded
442 comparable results in the absence of the paxillin N-terminus (Fig. 8b,c). The swapping of citrine
443 fragments between the PM probe and paxillin/LIMs (Supplementary Fig. 1c) produced analogous
444 outcomes, confirming the preferred complementation of the PM-localized CN fragment by C-
445 terminally over N-terminally CC-tagged paxillin/LIMs proteins (Supplementary Fig. 1d).
446 Interestingly, despite the general distribution of the PM-anchored citrine fragments within the lipid
447 bilayer (Supplementary Fig. 1f), the BiFC-driven paxillin-PM association identified in virtue of the
448 citrine fluorescence, did not affect the specific FA-localization of paxillin (Fig. 8c). On the other
449 hand, in the few cells that showed an interaction between the N-terminus of LIMs and the PM probe,
450 the BiFC signals was mainly localized in the PM outside of FAs (Supplementary Fig. 1g), suggesting
451 that when trapped in an “inverted” orientation, LIM domains have a low affinity for FAs
452 (Supplementary Fig. 1h).

453 To gather further insights about the mechanism of paxillin binding to the FA-complex, we mapped
454 the relative position of the paxillin extremities compared to the $\beta 3$ integrin tail, applying a similar
455 BiFC strategy (Fig. 8a). Efficient complementation of CC-tagged $\beta 3^{\text{WT}}$ integrin was obtained only
456 when the matching citrine fragment was fused to the C-terminus of paxillin (Fig. 8d,e). Similarly, the
457 BiFC efficiencies of the LIMs-only constructs were comparable to that of the corresponding full-
458 length protein (Fig. 8d,e), and insensitive to the swapping of the complementary citrine fragments
459 (Supplementary Fig. 1c), demonstrating the significantly higher interaction of the paxillin C-terminus
460 with the integrin cytoplasmic tail (Supplementary Fig. 1d).

461 Although the sliding of $\beta 3^{\text{VE/YA}}$ adhesions was rescued by directly joining paxillin and the integrin
462 receptor *via* BiFC (Fig. 1i and Supplementary Fig. 1b), it is still controversial whether paxillin
463 mediates FA stabilization by direct β integrin binding^{21,49,50}. We therefore asked whether an integrin-
464 independent binding of paxillin could also rescue the sliding of $\beta 3^{\text{VE/YA}}$ adhesions. Leveraging the
465 newly disclosed knowledge about the structural organization of adhesion complexes, an alternative,
466 LIM4-mediated paxillin-FA interaction was stabilized, in order to evaluate its potential to rescue FA-
467 sliding. The irreversible anchoring of LIM4 to the PM was achieved by using the SpyTag/SpyCatcher
468 technology⁶⁴ as presented in Fig. 8f. Upon co-expression of mCherry_paxillin_SpyTag and
469 PM_SpyCatcher a spontaneous reaction results in a stable isopeptide bond, which covalently
470 conjugated the two recombinant proteins (Fig. 8f). By this method, paxillin was depleted from the
471 cytoplasm, in favor of an enhanced PM localization (Supplementary Fig. 1i), which induced a slower
472 recovery in FAs after photobleaching (FRAP) (Supplementary Fig. 1j,k). The longer half-life and the
473 increased immobile fraction of such PM-anchored paxillin in FAs, effectively demonstrated the
474 occurrence of the cross-linking reaction. The latter, likely prolonging paxillin residency time within
475 FAs, rescued the $\beta 3^{\text{VE/YA}}$ integrin instability (Fig. 8g) and suggested that paxillin stability in adhesions
476 is a key factor in activating the clutch between the substrate-bound integrin and the retrogradely
477 moving F-actin network. Interestingly, strengthening paxillin binding to the PM compensate for the
478 loss of paxillin binding to $\beta 3$ integrin ($\beta 3^{\text{VE/YA}}$).

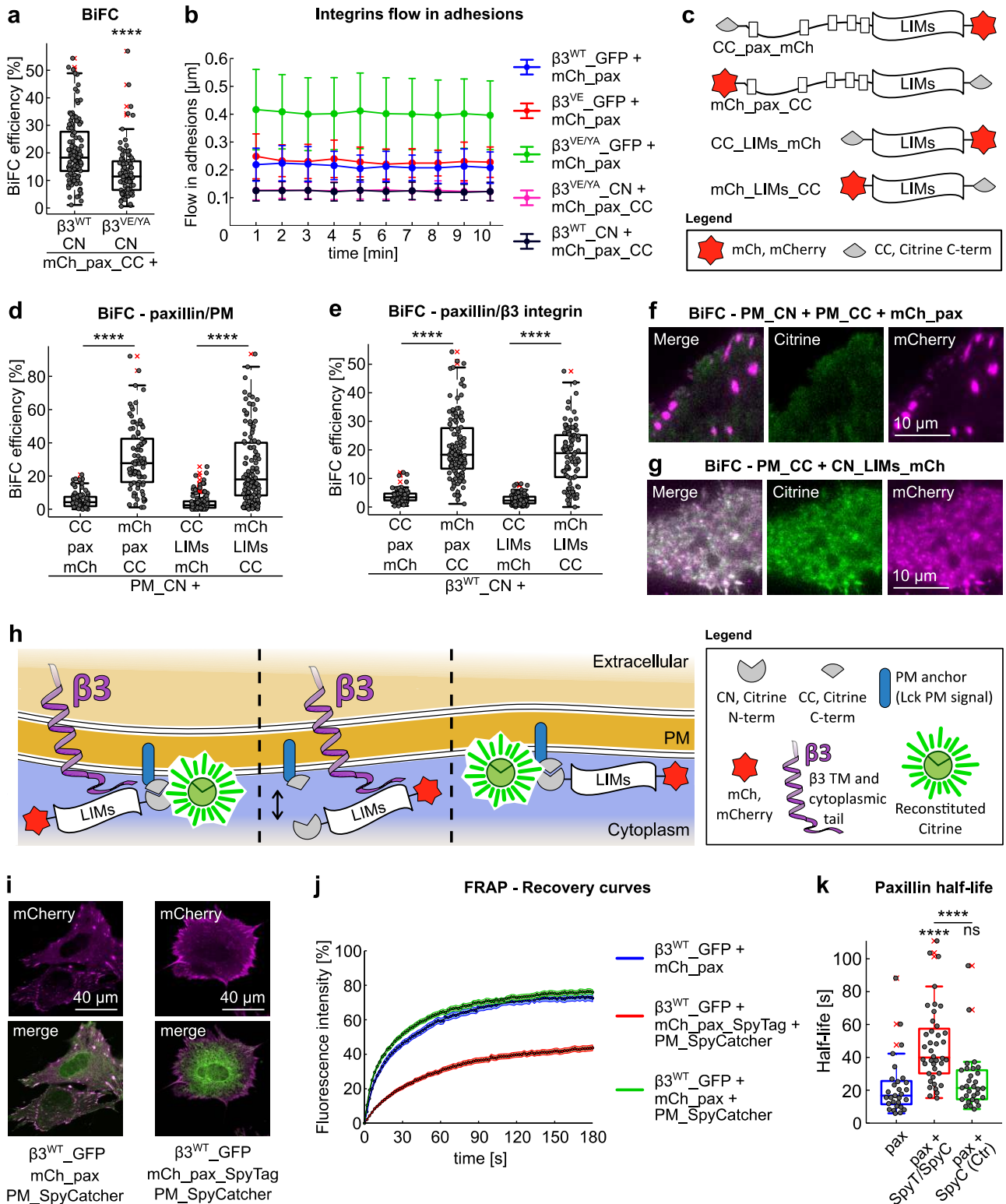


479

480 **Figure 8 – Preferential orientation of the paxillin LIM domains within FAs.** (a) Overview of the
 481 molecules tested with the BiFC assays and a summary outcome, in terms of citrine fluorescence,
 482 of their pairwise expression. (b,d) Quantification of the BiFC signal generated by the co-expression of
 483 each of the paxillin constructs shown in figure a with (b) the plasma membrane-localized CC
 484 fragment, in Swiss-3T3 or with (d) the β 3^{WT} C-terminally tagged with CC, in NIH-3T3 cells.
 485 Statistical analysis is provided in Supplementary Table 1. (c,e) Representative TIRF images of

486 experiments quantified in **b** and **d**. **(f)** Schematic representation of the functioning
487 SpyTag/SpyCatcher technology ⁶⁴ and of how it has been used in our cellular system. **(g)**
488 Quantification of the integrins flow in adhesions, expressed as mean displacement over time
489 ($\mu\text{m}/\text{min}$) per replicate. Statistical analysis is provided in Supplementary Table 2.

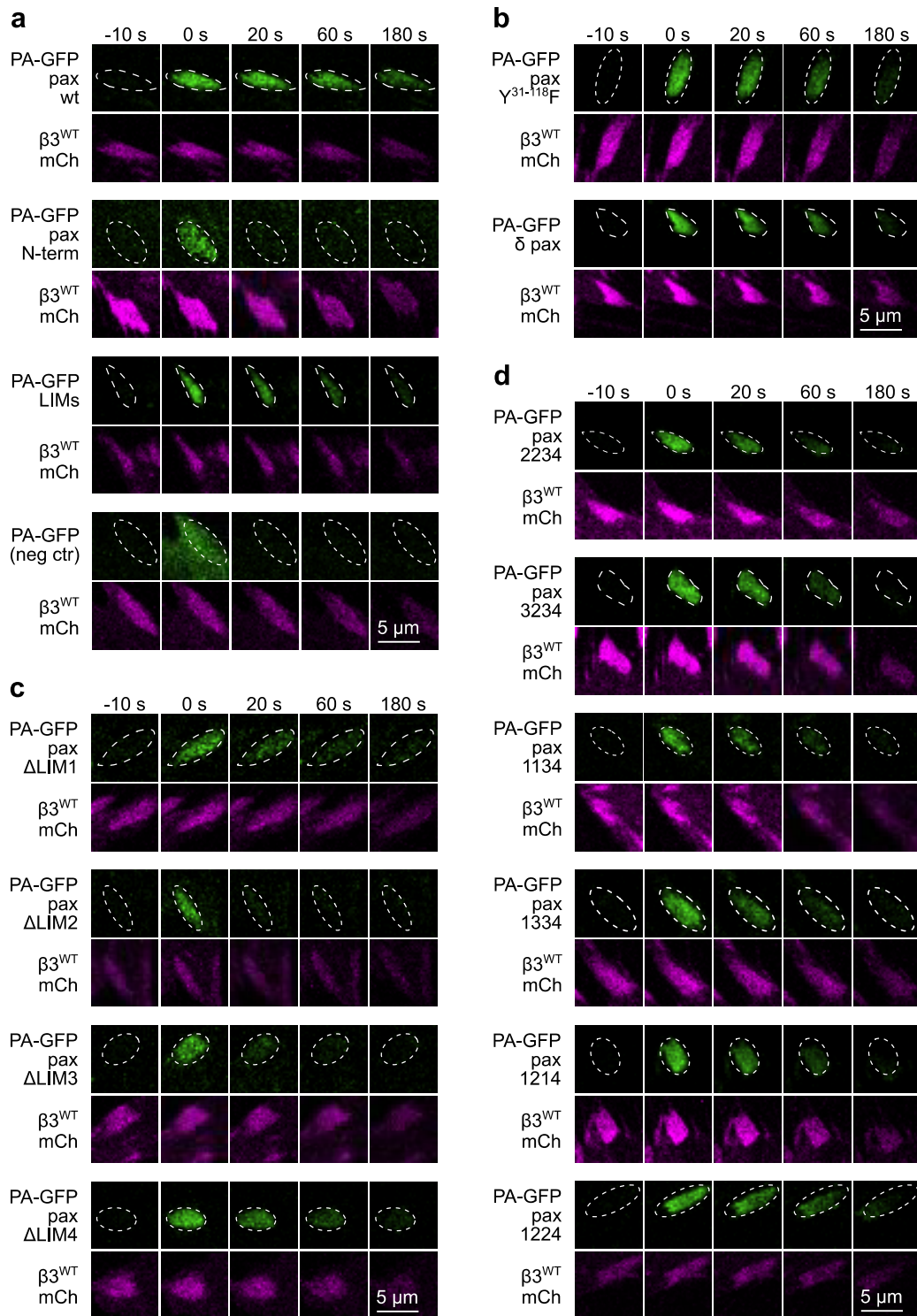
490 **Supplementary**



491

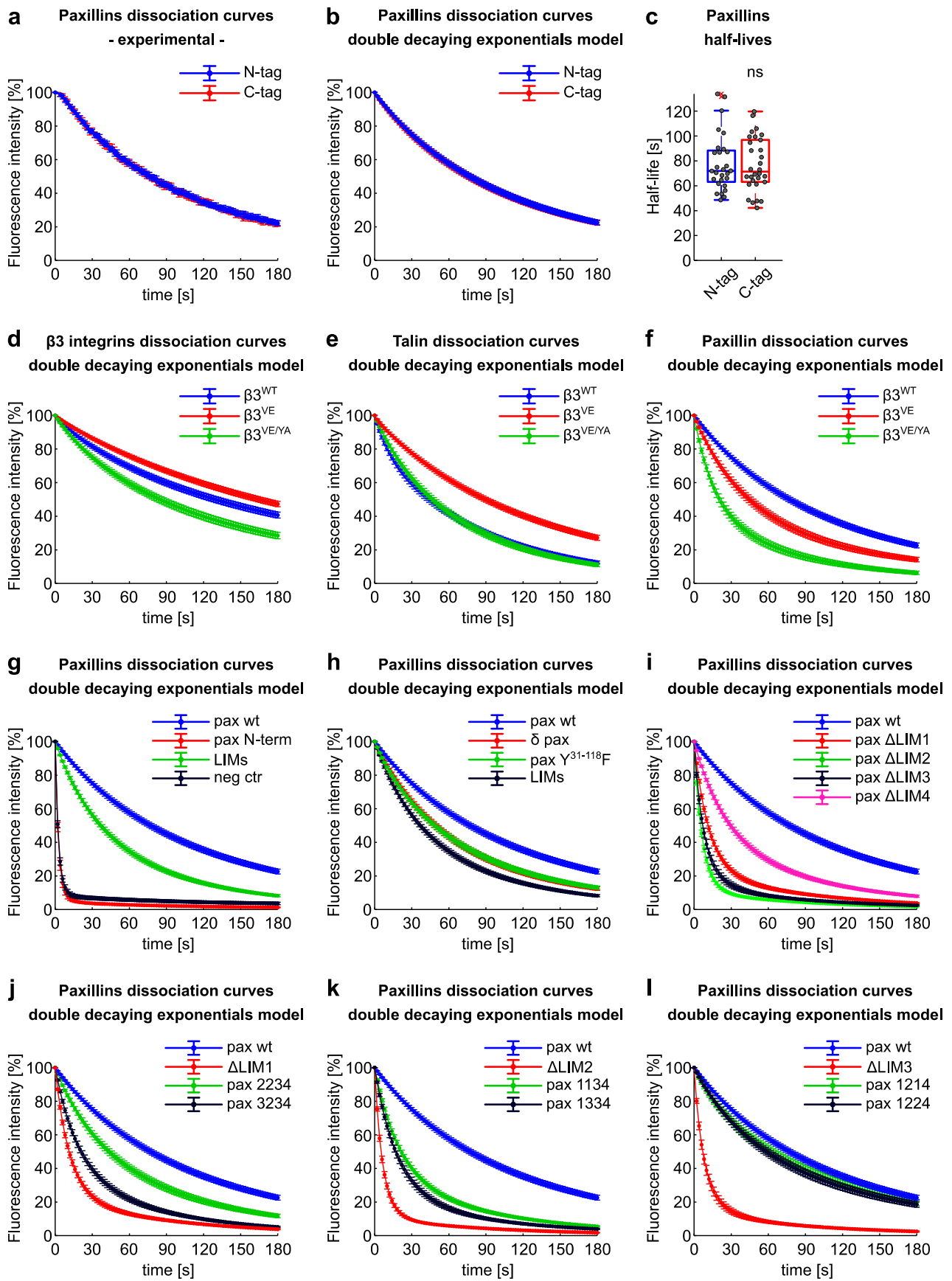
492 **Supplementary Figure 1 – BiFC and SpyTag/SpyCatcher assays to study focal adhesions**
 493 **organization and function.** (a) Quantification of the BiFC efficiency upon co-expression of
 494 mCherry_paxillin_CC and $\beta 3^{WT_CN}$ or $\beta 3^{VE/YA_CN}$ in NIH-3T3 cells. Statistical analysis is provided
 495 in Supplementary Table 1. (b) Quantification of the $\beta 3$ integrins flow in adhesions, expressed as
 496 displacement over time. Error bar $\pm SD$. Statistical analysis is provided in Supplementary Table 2. (c)
 497 Paxillin and LIMs fusion proteins tagged with mCherry and the citrine C-terminal fragment, tested

498 in BiFC assays with alternatively PM_CN or $\beta 3^{WT}$ _CN. **(d,e)** Quantification of the BiFC signal
499 generated by the co-expression of each of the paxillin constructs shown in figure c with **(d)** the plasma
500 membrane-localized CN fragment, in Swiss-3T3 or with **(e)** the $\beta 3^{WT}$ integrin C-terminally tagged
501 with CN, in NIH-3T3 cells. Statistical analysis is provided in Supplementary Table 1. **(f)**
502 Representative TIRF images of a triple positive Swiss-3T3 fibroblast, co-expressing
503 mCherry_paxillin and the two complementary citrine fragments, each one fused to the PM-targeting
504 peptide. While the BiFC signal is localized throughout to the plasma membrane, mCherry_paxillin
505 only appears in the discrete spots of FAs. Brightness and contrast automatically optimized. **(g)**
506 Example of a Swiss-3T3 fibroblast in which the co-expression of CN_LIMs_mCherry and PM_CC
507 led to substantial BiFC and concomitant mis-localization of LIMs. Brightness and contrast
508 automatically optimized. **(h)** Schematic representation of the possible scenarios, in terms of BiFC
509 generation, upon co-expression of CN-tagged LIMs recombinant proteins and the PM-localized
510 complementary citrine fragment. Left: the CN fragment at the C-terminus of LIMs leads to BiFC in
511 adhesions. Middle: the CN fragment in front of LIMs is not compatible with BiFC in adhesions.
512 Right: the CN fragment in front of LIMs can complement PM-localized CC outside adhesions. **(i)**
513 Differential paxillin distribution among FAs, cytosol and PM, in the absence (left) and in the presence
514 (right) of the irreversible fusion of the C-terminus to the PM_SpyCatcher. **(j)** Fluorescence Recovery
515 after Photobleaching (FRAP) of paxillin localized to $\beta 3^{WT}$ _GFP-positive FAs, in the absence
516 (mCherry_paxillin and mCherry_paxillin + PM_SpyCatcher, control) and in the presence
517 (mCherry_paxillin_SpyTag + PM_SpyCatcher) of the irreversible fusion of the C-terminus to the
518 PM_SpyCatcher. **(k)** Box plot of the half-lives of paxillin in $\beta 3^{WT}$ _GFP-positive FAs. Statistical
519 analysis is provided in Supplementary Table 3.



520

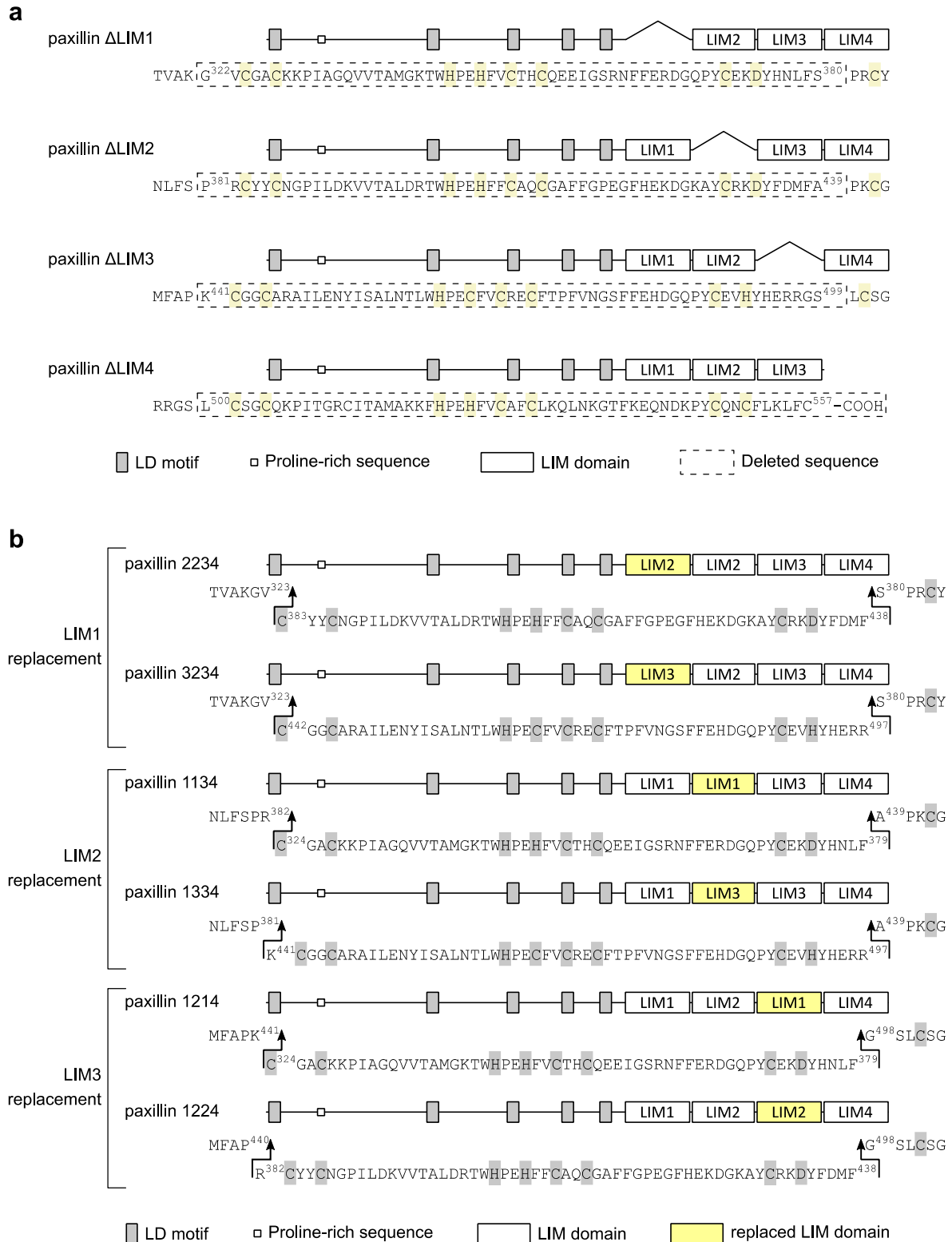
521 **Supplementary Figure 2 – Photoactivation time series of paxillin in $\beta 3^{\text{WT}}$ _mCherry-positive**
 522 **adhesions. (a-d)** Images of photoactivation time series of paxillin wt and mutants, transiently co-
 523 expressed with $\beta 3^{\text{WT}}$ _mCherry integrin in NIH-3T3 cells. Brightness and contrast of images in the
 524 green channel were adjusted to the image at t_0 . PA-GFP: photoactivatable GFP; mCh: mCherry.



525

526 **Supplementary Figure 3 – Fitting of double decaying exponential curves to experimental**
 527 **protein dissociation rates.** (a) Experimental dissociation curves of PA-GFP_paxillin (N-tag) and
 528 paxillin_PA-GFP (C-tag) from $\beta 3$ _mCherry-positive FAs. (c) Box plot of the half-lives of PA-

529 GFP_paxillin (N-tag) and paxillin_PA-GFP (C-tag) in β_3 _mCherry-positive FAs. Statistical analysis
 530 is provided in Supplementary Table 3. **(b,f-l)** Theoretical model of dissociation of PA-GFP-tagged
 531 paxillin proteins from β_3 _mCherry-positive FAs. **(d,e)** Theoretical model of dissociation of **(d)**
 532 β_3 _PA-GFP integrins from mCherry_paxillin-positive FAs and of **(e)** PA-GFP_talin from
 533 β_3 _mCherry-positive FAs.



534

535 **Supplementary Figure 4 – LIM deletion and replacement strategies.** **(a)** Schematic representation
 536 of the paxillin deletion mutants, showing the exact amino acid sequence deleted. **(b)** Schematic
 537 representation of the paxillin mutants obtained by the LIM domain replacement strategy. From the

538 top line: replacements of LIM1, replacements of LIM2 and replacements of LIM3. The exact
539 boundaries used for the replacement are shown in the sequences.

540 **Supplementary Movies 1-3 – Live cell imaging of adhesions of NIH-3T3 fibroblasts.**

- 541 - **Movie 1** NIH-3T3 co-expressing $\beta 3^{\text{WT}}$ _GFP and mCherry_paxillin.
- 542 - **Movie 2** NIH-3T3 co-expressing $\beta 3^{\text{VE/YA}}$ _GFP and mCherry_paxillin.
- 543 - **Movie 3** NIH-3T3 co-expressing $\beta 3^{\text{VE/YA}}$ _CN and mCherry_paxillin_CC.

544 mCh: mCherry; CN: citrine N-terminal fragment; CC: citrine C-terminal fragment.

545 **Supplementary Tables 1-4 – Statistical analysis.**

- 546 - **Table 1** Statistical analysis of BiFC experiments.
- 547 - **Table 2** Statistical analysis of the integrin flow in adhesions.
- 548 - **Table 3** Statistical analysis of photoactivation and FRAP experiments.
- 549 - **Table 4** Statistical analysis of FA-isolation experiments.

550 **Discussion**

551 **A stepwise recruitment of paxillin to focal adhesions**

552 The unique combination of molecular and cellular biological tools revealed that the LIM-dependent
553 localization of paxillin to FAs²¹ is the result of a synergistic binding to the PM and other FA
554 components. Although the N-terminal domain of paxillin is not contributing to the targeting
555 mechanism, it further stabilizes paxillin within FAs, when recruited there by the LIM-array. This
556 additional stabilization largely relies on phosphorylation of Y³¹ and/or Y¹¹⁸, which potentially
557 exposes LD motifs, further supporting the cross-linking to FAs proteins, such as talin¹⁶, FAK^{21,57},
558 and/or vinculin^{10,21,58,59}. Since the N-terminal domain prolonged paxillin half-life over that of talin,
559 it is likely that the paxillin N-terminus interacts with neighboring integrin/talin units, as proposed in
560 the slanted fence model of FAs¹.

561 **The focal adhesion targeting functions of the paxillin LIM1-LIM2-LIM3 array**

562 The LIM domain replacement strategy revealed the crucial role of paxillin LIM2 domain for its FA-
563 docking. As previously proposed for other LIM domain-proteins^{24,47}, specific residues confer to
564 distinct LIM domains exclusive functions and determine the selection of precise binding partners.
565 Based on our results, we propose that the deletion or the structural disruption of a LIM domain²¹
566 alters the distance between the remaining domains, undermining multiple synergistic interactions of
567 the LIMs-array with FAs, resulting in a cumulative binding defect. Indeed, the extension of the linker
568 sequence between LIM domains can abrogate a proper protein localization to adhesions⁶⁵, suggesting
569 that serial LIM domain modules must have a given relative position to be properly anchored to this
570 complex³¹.

571 Previous results supported an interaction of the paxillin LIM domains with the Y⁷⁴⁷ sidechain, situated
572 in the membrane-proximal NPLY⁷⁴⁷ motif of β 3 integrin^{30,41-43,48}. Although the dissociation rate of
573 paxillin carrying an inactive LIM2 domain (paxillin 1334) was almost exactly that of paxillin wt
574 dissociating from the β 3^{VE/YA} integrin-containing adhesions (Fig. 2g,h and 6d,e), we have no
575 structural or biochemical proof that could indicate an interaction between Y⁷⁴⁷ of integrin and the
576 LIM2 domain of paxillin. Interestingly, the binding of the LIM domains of the Enigma protein to
577 NPLY-like peptides^{47,48} was prevented by mutations analogous to our Y⁷⁴⁷A substitution⁴⁷. An
578 alternative binding mechanism of the paxillin LIM1-LIM2-LIM3 array to FAs could involve the
579 recognition of tandem LIM domains by extended peptides of the β 3 integrin tail, in a complex similar
580 to that proposed for LIM domain-containing transcription factors²⁷.

581 Recently, based on lysine cross-linking experiments, interactions between the N-terminal LD motifs
582 of paxillin and the PH and F0 domains of kindlin-2, as well as between the F0 domain and the paxillin
583 LIM3-LIM4 domains, have been identified and proposed to be responsible for paxillin recruitment to
584 FAs³⁶. However, none of these elements was strictly required for paxillin targeting and binding to
585 adhesions (Fig. 4b-e LIMs, Fig. 5 paxillin Δ LIM4, and Fig. 6f,g paxillin 1214 and paxillin 1224).
586 Even though the interaction with kindlin might be relevant for paxillin recruitment, it is probably not
587 the major factor for a stable docking to focal adhesions.

588 **LIM4 domain induces plasma membrane association of paxillin**

589 The local lipid composition of the PM influences the mobility of integrins, clustering and ligand
590 binding^{4,45,66}, and acts as an anchoring point for indispensable structural FA adapters, such as talin
591^{67,68} and kindlin^{69,70}. Additionally, transiently recruited paxillin-binding FA-proteins, such as FAK,
592 require membrane interaction and a precise orientation for their activity^{71,72}. Likewise, a PM-
593 dependent transient docking could be crucial for paxillin, which was identified as a membrane-
594 proximal protein by proximity biotinylation assays⁷³. Moreover, Qin and co-workers recently solved
595 the NMR structure of the kindlin-2 F0/paxillin LIM4 complex³⁸, which interaction could be part of
596 a kindlin-dependent mechanism of paxillin recruitment to the PM. Interestingly, such an interaction
597 with kindlin does not preclude the binding we propose between paxillin LIM4 and the PM. Consistent
598 with the hypothesis of a paxillin-PM interaction, we demonstrated paxillin palmitoylation (Fig. 7d).
599 However, the presence of 24 cysteines within the paxillin LIM domains and the limited possibility of
600 mutagenesis to preserve the double zinc-finger folding, hindered the identification of the paxillin
601 palmitoylation site(s). Nevertheless, the almost exclusive BiFC between the C-terminus of paxillin
602 and the PM-localized probe (Fig. 8b,c and Supplementary Fig.1d), accredited our hypothesis.
603 Importantly, the paxillin orientation within FAs relied on the LIMs-array, showing that the precise
604 organization of these domains matters for paxillin docking to FA.

605 **The β 3 integrin-talin-paxillin complex**

606 Within the elaborated network of (synergistic) bonds established among FA-proteins, paxillin is
607 among the most connected elements⁷⁴. Together with talin and kindlin, paxillin belongs to the
608 structural subnet that connects integrin receptors to the actin cytoskeleton⁷⁴. However, so far, it has
609 been only described as an adaptor or scaffold protein¹⁷. Nevertheless, the uncoupling of paxillin from
610 the binomial β 3 integrin/talin interaction (β 3^{VE/YA}), produced FAs with structural defects, which could
611 be rescued by the reintroduction of the LIMs-array. Importantly, our data revealed that the
612 mechanically stable incorporation of paxillin into integrin-containing FAs is distinct from the

613 mechanism of paxillin recruitment to the FA-microenvironment (Fig. 6h-k). This stepwise model of
614 paxillin recruitment and docking may involve a transient stabilization by the proposed LIM4-PM
615 interaction ⁷⁵. The latter could also account for the paxillin localization to Mn²⁺-induced integrin-
616 kindlin clusters in the absence of talin, which impaired maturation is reminiscent of the unstable
617 $\beta 3^{VE/YA}$ adhesions phenotype ³⁷. Indeed, paxillin binding to the adhesion complex also reduces the
618 exchange rate of $\beta 3$ integrins between immature and F-actin coupled integrin-talin clusters ⁴⁵, as well
619 as the dynamic assembly/disassembly of FAs ⁵¹.

620 Altogether, our data highlighted the need of comprehensive and integrating studies, based on
621 complementary approaches, to understand the structural interactions required for the physiological
622 functioning of focal adhesions, both at the level of the assembly of the focal adhesion, and its
623 mechanosensing and signal transduction.

624 **Material and methods**

625 **Cell culture and transient transfection**

626 NIH-3T3 and Swiss-3T3 fibroblasts were grown at 37 °C (10% CO₂) in DMEM with 4500 mg/L
627 glucose (Sigma-Aldrich), supplemented with 10% heat inactivated FBS (PANBiotech), 1%
628 penicillin-streptomycin (Gibco) and 2 mM glutamine (Sigma-Aldrich). Transient transfections were
629 performed 24 hours after seeding cells, with jetPRIME (Polyplus Transfection) according to the
630 manufacturer's recommendations.

631 **2-bromopalmitate treatment and Acyl-Resin Assisted Capture (Acyl-RAC)**

632 Protein S-acylation was analyzed by the Acyl-RAC assay as described (Gadalla, Abrami, and Goot
633 2020), with some modifications. 4 hours after transfection, samples were split in two and treated with
634 DMSO or 2-bromopalmitate at 60 μM. 24 hours after transfection, cells were trypsinized, washed
635 with cold PBS and lysed in 300 μl of lysis buffer (1.5% Triton-X100, 25 mM HEPES, 1 mM EDTA
636 in 8 M urea solution supplemented with protease inhibitor cocktail). To block free SH groups with S-
637 methyl methanethiosulfonate (MMTS, Sigma 64306), one volume of 2× blocking buffer (200 mM
638 HEPES, 2 mM EDTA, 5% SDS and 2.2% MMTS in 8 M urea solution supplemented with protease
639 inhibitor cocktail) was added to the cell lysate and incubated, protected from light, for 5 h at 42 °C in
640 a shaker (600 rpm). Next, proteins were precipitated adding ice-cold methanol and chloroform (4/4/1
641 : protein mixture/methanol/chloroform), followed by centrifugation at 14000 rpm for 15 min at 4 °C.
642 The protein pellet was broken using a needle and washed four times with 600 μl of methanol. Air-
643 dried pellet was resuspended in 220 μl of 5× binding buffer (100 mM HEPES, 5 mM EDTA, and 5%
644 SDS in 8 M urea solution supplemented with protease inhibitor cocktail). Cell debris were removed
645 by centrifugation at 14000 rpm for 10 min at 4 °C. 5% of the solubilized pellet was saved as Total
646 Cell Lysate (TCE) to check for protein expression by western blotting. The remaining was diluted
647 with 8 M urea containing protease inhibitor cocktail, to reach a final volume of 1080 μl, and divided
648 into two tubes. Thioester bonds of one aliquot were cleaved with 600 μl of hydroxylamine (HA,
649 Sigma 55459) freshly dissolved in water to 2.7 M and adjusted to pH 7.4. The control aliquot was
650 treated with equal amount of 2M Tris-base. Thiopropyl Sepharose® 6B beads (Sigma T8387) were
651 firstly activated for 1 h with mqH₂O, then resuspended in 3 volumes of binding buffer (100 mM
652 HEPES, 1 mM EDTA, and 1% SDS in 8 M urea solution supplemented with protease inhibitor
653 cocktail) and finally added to protein samples (200 μl each). Samples were light-protected and
654 incubated overnight at room temperature on a rotating wheel. Beads were then washed 5× in binding

655 buffer and bound proteins eluted from the beads with SDS-PAGE sample buffer (140 mM SDS, 20%
656 glycerol, 25% β -mercaptoethanol, and bromophenolblue) for 5 min at 95°C.

657 **Photoactivation-based experiments**

658 Image acquisition and analysis were performed at the Bioimaging Core Facility, Faculty of Medicine,
659 University of Geneva. Briefly, transfected NIH-3T3 cells were cultured overnight on glass bottom
660 coverslips. 1 hour before imaging, culturing medium was replaced with F12 medium (Sigma-
661 Aldrich), supplemented with FBS, penicillin/streptomycin and glutamine. Photoactivation was
662 performed on a Nikon A1r confocal laser scanning microscope equipped with a 60x oil immersion
663 objective and a 37°C and 5% CO₂ incubation chamber. Laser wavelengths of 488 nm and 561 nm
664 were used to acquire three pictures at 5 sec intervals before photoactivation and 1 frame every 2 sec
665 for 3 min after photoactivation. Excitation of photoactivatable GFP molecules was achieved by means
666 of a 405nm laser (10% power), on a single ROI matching the size of an mCherry-positive focal
667 adhesion. Using Imaris combined with MatLab scripts, we identified the area of photoactivation,
668 automatically repositioned it in case of lateral shift according to the mCherry signal and extracted the
669 mean green intensity within the ROI for each time point. The first three time points, corresponding
670 to the background, were averaged and subtracted from the full-time course. The intensity of the first
671 acquisition after photoactivation was set to “100% intensity”, and all other values were calculated as
672 ratio. For each photoactivation time series, a constrained double decaying exponentials model
673 (decreasing form) with the formula $(\bar{F}_0 - c)(k_{fast}e^{-\lambda_{fast}t} + (\bar{F}_0 - k_{fast})e^{-\lambda_{slow}t}) + c$ was use to
674 fit the data points. For each of them, the half-life was defined as the time needed to lose 50% of the
675 intensity at time 0, shown in the box and whisker plot, and used for statistical comparison. The same
676 constrained double decaying exponentials model was also used to fit the average data, offering a
677 visual inspection of the goodness of the fit (theoretical model).

678 **Florescence Recovery After Photobleaching - FRAP**

679 FRAP was conducted similarly to photoactivation experiments. However, seeding of transfected cells
680 on coverslips was performed 4 hours after transfection to avoid prior irreversible binding of paxillin
681 to the PM *via* SpyTag/SpyCatcher. Time intervals of acquisition were maintained, while the
682 photoactivation step was replaced by 3 rounds of scanning using the laser wavelength of 561 nm at
683 100% power, which efficiently bleached the mCherry fluorophore localized within the selected
684 adhesion. The residual fluorescence was subtracted from the entire time curse, the first three
685 acquisitions, corresponding to the mCherry level prior to bleaching, were averaged and set to 100%
686 intensity, while all other values were calculated as ratio. Individual replicates were fitted with a

687 constrained double exponentials model (increasing form) with the formula $\bar{F}_{fast}(1 - e^{-\lambda_{fast}t}) +$
688 $\bar{F}_{slow}(1 - e^{-\lambda_{slow}t})$. The theoretical half-lives thereof calculated were presented in box and whisker
689 plots and used for statistical comparison.

690 **Isolation of focal adhesions, immunostaining and TIRF microscopy**

691 After culturing cells overnight on coverslips, FAs were isolated by means of a protocol previously
692 described (Kuo et al. 2012) and immediately fixed with 4% PFA/PBS. For immunostaining, isolated
693 complexes were blocked for 30 min with a solution of PBS containing 1% BSA, incubated for 60 min
694 with the primary antibody and subsequently for 45 min with the corresponding secondary antibody,
695 both diluted in the same buffer. Images were acquired on a Nikon Eclipse Ti equipped with a 100x
696 oil immersion objective. TIRF angle and lasers intensities were kept constant for all experiments. For
697 each image acquired, a custom Metamorph journal was used to identify adhesions on the green
698 channel and subsequently to extract the mean intensity for each of the laser wavelengths used. The
699 quantification of the capacity of cytosolic proteins to be retained in the isolated FAs was expressed
700 in respect to the residual integrin fluorescence, thus as a red/green ratio. In the case of antibody
701 staining, to compensate for possible variations among experiments, the mean red/green ratio in $\beta 3^{WT}$
702 integrin adhesions was always considered equal to 1, and therefore all the measures expressed in
703 respect to it.

704 **Bimolecular Fluorescence Complementation (BiFC)**

705 The citrine fluorophore (FPbase ID VR7EN), generated by the Q⁶⁹M mutation within the YFP
706 sequence, was obtained as previously described (Paulhe et al. 2009). The N-terminal (CN, aa 1-173)
707 and the C-terminal (CC, aa 174-239) fragments were cloned upstream or downstream the coding
708 sequences of our proteins of interest.

709 For BiFC assays, transfected cells were seeded on glass coverslips 4 hours after transfection and fixed
710 with 4% PFA/PBS 48 hours later. Images were acquired on a Nikon Eclipse Ti equipped with a 100x
711 oil immersion objective. TIRF angle and lasers intensities were kept constant for all experiments.
712 Images were processed with Metamorph, as explained above for isolated FAs, with the only
713 difference that adhesions were identified in virtue of their red fluorescence instead of the green one.
714 For the quantification of the BiFC efficiency, the first step consisted of determining the green
715 background, corresponding to the mean green intensity in mCherry-positive FAs measured by
716 applying the just described analysis to NIH-3T3 and Swiss-3T3 cells only expressing the
717 CN_paxillin_mCherry construct. This value was then subtracted from the mean green intensity in
718 adhesions of each image acquired upon co-expression of pair of BiFC probes. The resulting green

719 value was divided by the red mean intensity in adhesions of the same image. Finally, this ratio was
720 compared to the one obtained by expressing solely the corresponding paxillin/LIMs construct
721 presenting the full-length citrine in place of the CN/CC fragment (and analyzed in the same way)
722 considered to be the maximal, 100%, efficiency that could be reached.

723 **Integrin flow in adhesions**

724 As for BiFC assays, cells were seeded on coverslips 4 hours after transfection. Two days later, the
725 culturing medium was replaced with F12 medium (Sigma-Aldrich), supplemented with FBS,
726 penicillin/streptomycin and glutamine, and cells were imaged by means of a Nikon A1r confocal laser
727 scanning microscope equipped with a 60x oil immersion objective and a 37 °C and 5% CO₂
728 incubation chamber. Laser wavelengths of 488 nm and 561 nm were used to acquire 1 frame every
729 minute for a total of 10 minutes. Adhesions of a given cell, were segmented frame by frame, using
730 the neurite function of Metamorph applied on the (mCherry) paxillin-derived fluorescence channel.
731 Thereafter, Matlab was used to correct the possible translational drifts of cells, and their respective
732 adhesion masks, occurring during the time course of the acquisition. Then background subtraction,
733 followed by a non-local means filter was used to diminish the contribution of spatially stationary
734 areas, i.e. mainly outside of adhesions. Dense optical flow was estimated for all the pixels in the
735 frames, using the Farneback's method ⁷⁶. The velocity of the adhesions flow was computed as the
736 average magnitude of the flow within the adhesion mask between two following frames.

737 **Statistics**

738 BiFC data did not consistently satisfy normal distribution and therefore statistical comparison was
739 performed using the Wilcoxon test based on ranks. For comparison among more than two groups the
740 Kruskal-Wallis extension was applied. Significant differences among proteins retained in isolated
741 FAs were analogously evaluated. Differences of integrins flows in adhesions among time points or
742 between samples were assessed by one-way Anova test. The half-lives calculated from FLAP data
743 were subject to one-way Anova test, while for half-lives calculated from FRAP experiments the
744 Kruskal-Wallis test was employed. All multiple comparisons were followed by Tukey-Kramer post-
745 hoc correction. The nomenclature used in figures is based on the following criteria: ns (not
746 significant) $p > 0.05$; *, $p < 0.05$; **, $p < 0.01$; ***, $p < 0.001$; ****, $p < 0.0001$. For each experiment,
747 sample size, complete statistical analysis and p values are provided in tables in *supplementary dataset*.
748 All experiments were repeated at least three times and no repeated measurements were performed.
749 For all box and whisker plots presented in this manuscript the box shows the median, 25th and 75th
750 percentiles, while the whiskers the maximum and minimum values. Outliers are indicated with the

751 symbol x . FLAP data are shown as mean intensity \pm standard error of the mean (experimental) or
752 constrained double decaying exponentials model \pm standard error of the mean (theoretical
753 dissociation model). For FRAP experiments, the mean value for each time point is represented with
754 a dot, the standard error of the mean with a colored background and the fitting of the double
755 exponential function to the mean values with black a curve.

756 **cDNAs and site-directed mutagenesis**

757 The cDNA encoding the full-length, wild-type and mutant, mouse β 3 integrins were obtained from
758 the previously described integrin fusion proteins (Pinon et al. 2014). The linker, coding for the
759 sequence DGSPVAT and containing an AgeI site, was introduced in between the integrin sequence
760 (Uniprot identifier O54890-1) and the fluorescent protein (either GFP, mCherry, PA-GFP or citrine
761 fragments).

762 Paxillin fusion proteins were expressed in a cytomegalovirus promoter-driven pcDNA3 vector. All
763 residues of paxillin recombinant proteins were numbered according to the human paxillin α (Uniprot
764 identifier P49023-2). Paxillin N-terminus and LIMs constructs were obtained by the cloning of a
765 PCR-amplified fragment of full-length paxillin, either corresponding to the first 322 amino acids or
766 to the C-terminal sequence starting from residue 317. Paxillin LIM domain deletion mutants were
767 obtained by overlap extension PCR, producing the deletion shown in Supplementary Fig. 4a, and here
768 summarized. Paxillin Δ LIM1: deletion of aa 322-380; paxillin Δ LIM2: deletion of aa 381-439;
769 paxillin Δ LIM3 deletion of aa 441-499; paxillin Δ LIM4 truncation from aa 500. Point mutations were
770 introduced by site-directed mutagenesis. For the LIM domain replacement strategy, we either used
771 serial overlap extension PCRs with degenerated primers or cloned a *de novo*-synthesized nucleotide
772 sequence, coding for the LIM domain of interest but with a degenerated codons compared to the
773 original one. The amino acid sequence of the final recombinant proteins is shown in Supplementary
774 Fig. 4b. In summary, in paxillin 2234 the aa 324-379 were replaced by the sequence found at aa 383-
775 438; in paxillin 3234 the aa 324-379 were replaced by the sequence found at aa 442-497; in paxillin
776 1134 the aa 383-438 were replaced by the sequence found at aa 324-379; in paxillin 1334 the aa 382-
777 438 were replaced by the sequence found at aa 441-497; in paxillin 1214 the aa 442-497 were replaced
778 by the sequence found at aa 324-379; and in paxillin 1224 the aa 441-497 were replaced by the
779 sequence found at aa 382-438. The C-terminally tagged paxillins (paxillin_PA-GFP and paxillin
780 proteins for BiFC and SpyTag/SpyCatcher assays) were obtained by removing the stop codon in a
781 PCR step, and then joining the sequence coding for one of the tags *via* a linker coding for a GPVAT
782 peptide, containing an AgeI site.

783 The PM-anchored proteins were obtained by sequential cloning of the sequences coding for the PM-
784 targeting peptide of Lck (MGCVCSSNPEL) and the citrine fragment (either CN or CC), or the
785 SpyCatcher, into a pCDNA3 vector. The plasma membrane-targeting sequence was recovered from
786 the Lck-mScarlet-I (98821; Addgene; deposited by D. Gadella)⁷⁷, a gift from N. Gauthier (IFOM,
787 the FIRC Institute for Molecular Oncology, Milan, Italy).

788 PA-GFP_talin was obtained by replacing the ECFP with the PA-GFP fluorophore, in the chimeric
789 full-length construct previously described (Saltel et al. 2009).

790 The amino acids compositions of the fluorescent proteins can be found in the FPbase database, at the
791 following IDs. Photoactivatable GFP (PA-GFP): FPbase ID 7QYHY (gift from Christoph Ballestrem,
792 Wellcome Trust Centre for Cell-Matrix Research, University of Manchester, Manchester, UK)⁷⁸;
793 mCherry: FPbase ID ZERB6; citrine: FPbase ID VR7EN. SpyTag/SpyCatcher003 sequences can be
794 found in the Addgene repository⁶⁴.

795 DNA sequence analysis was performed for all constructs and mutants to ensure error-free
796 amplification and correct base replacement.

797 **Protein extraction and western blotting**

798 NIH-3T3 transiently transfected were trypsinized and lysed with Ripa buffer (150 mM NaCl, 5 mM
799 EDTA, 25 mM Tris-HCl pH 7.6, 1% Triton X-100, 1% sodium deoxycholate, 0.1% SDS, 1 mM
800 PMSF, and 1 µg/ml chymostatin, leupeptin, antipain, and pepstatin; all obtained from Sigma-Aldrich)
801 during 30 min on ice. Cell lysates were then cleared by a 30 min centrifugation at 14000 rpm and at
802 4 °C, supplemented with SDS sample buffer 4× (140 mM SDS, 20% glycerol, 25% β-
803 mercaptoethanol, and bromophenolblue) and boiled for 5 min. Samples were resolved by SDS-PAGE
804 and transferred to nitrocellulose membranes (GE Healthcare). Membrane were blocked in 5% (w/v)
805 BSA (A1391 Applichem) diluted in TBST buffer (0.5 m Tris-base, 1.5 M NaCl, 0.1% Tween 20, pH
806 7.6), then incubated with primary antibody followed by horseradish peroxidase (HRP)-conjugated
807 secondary antibody, both diluted in 5% BSA TBST buffer. Staining were revealed using Advansta
808 ECL Quantum (K-12042) or Sirius (K-12043) substrates.

809 **Reagents**

810 Purified mouse monoclonal anti-paxillin (BD Biosciences 610051). Mouse monoclonal anti-vinculin
811 (Sigma-Aldrich V9131). Rabbit polyclonal anti-caveolin-1 (Santa Cruz Biotechnology sc-894).
812 Rabbit polyclonal anti-mCherry (BioVision 5993-30T). Alexa Fluor 555 anti-mouse (ThermoFisher

813 A-31570). Alexa Fluor 633 anti-mouse (ThermoFisher A-21050). HRP-conjugated anti-mouse
814 (Jackson). HRP-conjugated anti-rabbit (Jackson).

815 **Acknowledgments**

816 We are grateful to Dr. Sunil Dogga for introducing us to the Acyl-RAC technique and to Dr. Patricia
817 Vazquez for her contribution in the initial phase of this work. We thank Prof. Vesa Hytönen, Latifeh
818 Azizi and Paula Turkki for helpful discussions and providing the SpyTag/SpyCatcher cDNAs. We
819 are grateful to all the members of the Bioimaging core facility of the Centre Médical Universitaire
820 for help in microscopy and image analysis. This work was supported by the Swiss National Science
821 Foundation, grants 31003A_166384 and 310030_185261. The authors declare no competing financial
822 interests.

823 **Author contributions**

824 MR and BWH designed the DNA constructs and experiments. MR conducted the experiments. NL
825 designed the strategy to analyze the photoactivation and FRAP data and the integrin flow in
826 adhesions. MR and BWH wrote the manuscript. All authors accepted the final version of the
827 manuscript.

828 **Data availability**

829 All microscopy images shown or analyzed in this work are deposited at University of Geneva and are
830 available upon request.

831 **Code availability**

832 Matlab and Metamorph codes were developed in-house at the Bioimaging Core Facility, Faculty of
833 Medicine, University of Geneva, and here deposited. Codes are available upon request.

834

835 **References**

- 836 1. Bachmann, M., Kukkurainen, S., Hytonen, V.P. & Wehrle-Haller, B. Cell Adhesion by
837 Integrins. *Physiol Rev* **99**, 1655-1699 (2019).
- 838 2. Kechagia, J.Z., Ivaska, J. & Roca-Cusachs, P. Integrins as biomechanical sensors of the
839 microenvironment. *Nat Rev Mol Cell Biol* **20**, 457-473 (2019).
- 840 3. Bachmann, M. et al. Induction of ligand promiscuity of alphaVbeta3 integrin by mechanical
841 force. *J Cell Sci* **133**(2020).
- 842 4. Wehrle-Haller, B. Structure and function of focal adhesions. *Curr Opin Cell Biol* **24**, 116-24
843 (2012).
- 844 5. Yu, C.H., Luo, W. & Sheetz, M.P. Spatial-temporal reorganization of activated integrins. *Cell*
845 *Adh Migr* **6**, 280-4 (2012).
- 846 6. Roca-Cusachs, P., Gauthier, N.C., Del Rio, A. & Sheetz, M.P. Clustering of alpha(5)beta(1)
847 integrins determines adhesion strength whereas alpha(v)beta(3) and talin enable
848 mechanotransduction. *Proc Natl Acad Sci U S A* **106**, 16245-50 (2009).
- 849 7. von Wichert, G., Haimovich, B., Feng, G.S. & Sheetz, M.P. Force-dependent integrin-
850 cytoskeleton linkage formation requires downregulation of focal complex dynamics by Shp2.
851 *EMBO J* **22**, 5023-35 (2003).
- 852 8. Webb, D.J. et al. FAK-Src signalling through paxillin, ERK and MLCK regulates adhesion
853 disassembly. *Nat Cell Biol* **6**, 154-61 (2004).
- 854 9. Changede, R., Xu, X., Margadant, F. & Sheetz, M.P. Nascent Integrin Adhesions Form on All
855 Matrix Rigidities after Integrin Activation. *Dev Cell* **35**, 614-621 (2015).
- 856 10. Case, L.B. et al. Molecular mechanism of vinculin activation and nanoscale spatial
857 organization in focal adhesions. *Nat Cell Biol* **17**, 880-92 (2015).
- 858 11. Kalappurakkal, J.M. et al. Integrin Mechano-chemical Signaling Generates Plasma
859 Membrane Nanodomains that Promote Cell Spreading. *Cell* **177**, 1738-1756 e23 (2019).
- 860 12. Weng, Z., Taylor, J.A., Turner, C.E., Brugge, J.S. & Seidel-Dugan, C. Detection of Src
861 homology 3-binding proteins, including paxillin, in normal and v-Src-transformed Balb/c 3T3
862 cells. *J Biol Chem* **268**, 14956-63 (1993).
- 863 13. Alam, T., Alazmi, M., Gao, X. & Arold, S.T. How to find a leucine in a haystack? Structure,
864 ligand recognition and regulation of leucine-aspartic acid (LD) motifs. *Biochem J* **460**, 317-
865 29 (2014).
- 866 14. Pasapera, A.M., Schneider, I.C., Rericha, E., Schlaepfer, D.D. & Waterman, C.M. Myosin II
867 activity regulates vinculin recruitment to focal adhesions through FAK-mediated paxillin
868 phosphorylation. *J Cell Biol* **188**, 877-90 (2010).
- 869 15. Tumbarello, D.A., Brown, M.C. & Turner, C.E. The paxillin LD motifs. *FEBS Lett* **513**, 114-
870 8 (2002).
- 871 16. Zacharchenko, T. et al. LD Motif Recognition by Talin: Structure of the Talin-DLC1
872 Complex. *Structure* **24**, 1130-41 (2016).
- 873 17. Deakin, N.O. & Turner, C.E. Paxillin comes of age. *J Cell Sci* **121**, 2435-44 (2008).
- 874 18. Frank, S.R. & Hansen, S.H. The PIX-GIT complex: a G protein signaling cassette in control
875 of cell shape. *Semin Cell Dev Biol* **19**, 234-44 (2008).
- 876 19. Turner, C.E. Paxillin and focal adhesion signalling. *Nat Cell Biol* **2**, E231-6 (2000).
- 877 20. Webb, D.J. et al. Paxillin phosphorylation sites mapped by mass spectrometry. *J Cell Sci* **118**,
878 4925-9 (2005).
- 879 21. Brown, M.C., Perrotta, J.A. & Turner, C.E. Identification of LIM3 as the principal
880 determinant of paxillin focal adhesion localization and characterization of a novel motif on
881 paxillin directing vinculin and focal adhesion kinase binding. *J Cell Biol* **135**, 1109-23 (1996).
- 882 22. Kadrmas, J.L. & Beckerle, M.C. The LIM domain: from the cytoskeleton to the nucleus. *Nat*
883 *Rev Mol Cell Biol* **5**, 920-31 (2004).

- 884 23. Velyvis, A., Yang, Y., Wu, C. & Qin, J. Solution structure of the focal adhesion adaptor
885 PINCH LIM1 domain and characterization of its interaction with the integrin-linked kinase
886 ankyrin repeat domain. *J Biol Chem* **276**, 4932-9 (2001).
- 887 24. Arber, S. & Caroni, P. Specificity of single LIM motifs in targeting and LIM/LIM interactions
888 in situ. *Genes Dev* **10**, 289-300 (1996).
- 889 25. Chiswell, B.P. et al. Structural basis of competition between PINCH1 and PINCH2 for
890 binding to the ankyrin repeat domain of integrin-linked kinase. *J Struct Biol* **170**, 157-63
891 (2010).
- 892 26. Gadd, M.S. et al. A structural basis for the regulation of the LIM-homeodomain protein islet
893 1 (Isl1) by intra- and intermolecular interactions. *J Biol Chem* **288**, 21924-35 (2013).
- 894 27. Matthews, J.M. & Potts, J.R. The tandem beta-zipper: modular binding of tandem domains
895 and linear motifs. *FEBS Lett* **587**, 1164-71 (2013).
- 896 28. Schmeichel, K.L. & Beckerle, M.C. The LIM domain is a modular protein-binding interface.
897 *Cell* **79**, 211-9 (1994).
- 898 29. Vaynberg, J. et al. Non-catalytic signaling by pseudokinase ILK for regulating cell adhesion.
899 *Nat Commun* **9**, 4465 (2018).
- 900 30. Sawada, Y. & Sheetz, M.P. Force transduction by Triton cytoskeletons. *J Cell Biol* **156**, 609-
901 15 (2002).
- 902 31. Schiller, H.B. & Fassler, R. Mechanosensitivity and compositional dynamics of cell-matrix
903 adhesions. *EMBO Rep* **14**, 509-19 (2013).
- 904 32. Schiller, H.B., Friedel, C.C., Boulegue, C. & Fassler, R. Quantitative proteomics of the
905 integrin adhesome show a myosin II-dependent recruitment of LIM domain proteins. *EMBO*
906 *Rep* **12**, 259-66 (2011).
- 907 33. Dawid, I.B., Breen, J.J. & Toyama, R. LIM domains: multiple roles as adapters and functional
908 modifiers in protein interactions. *Trends Genet* **14**, 156-62 (1998).
- 909 34. Smith, M.A. et al. LIM domains target actin regulators paxillin and zyxin to sites of stress
910 fiber strain. *PLoS One* **8**, e69378 (2013).
- 911 35. Wade, R. & Vande Pol, S. Minimal features of paxillin that are required for the tyrosine
912 phosphorylation of focal adhesion kinase. *Biochem J* **393**, 565-73 (2006).
- 913 36. Bottcher, R.T. et al. Kindlin-2 recruits paxillin and Arp2/3 to promote membrane protrusions
914 during initial cell spreading. *J Cell Biol* **216**, 3785-3798 (2017).
- 915 37. Theodosiou, M. et al. Kindlin-2 cooperates with talin to activate integrins and induces cell
916 spreading by directly binding paxillin. *Elife* **5**, e10130 (2016).
- 917 38. Zhu, L. et al. Structural Basis of Paxillin Recruitment by Kindlin-2 in Regulating Cell
918 Adhesion. *Structure* **27**, 1686-1697 e5 (2019).
- 919 39. Zhang, X. et al. Talin depletion reveals independence of initial cell spreading from integrin
920 activation and traction. *Nat Cell Biol* **10**, 1062-8 (2008).
- 921 40. Wixler, V. et al. The LIM-only protein DRAL/FHL2 binds to the cytoplasmic domain of
922 several alpha and beta integrin chains and is recruited to adhesion complexes. *J Biol Chem*
923 **275**, 33669-78 (2000).
- 924 41. Soto-Ribeiro, M. et al. beta1D integrin splice variant stabilizes integrin dynamics and reduces
925 integrin signaling by limiting paxillin recruitment. *J Cell Sci* **132**(2019).
- 926 42. Hytonen, V.P. & Wehrle-Haller, B. Mechanosensing in cell-matrix adhesions - Converting
927 tension into chemical signals. *Exp Cell Res* **343**, 35-41 (2016).
- 928 43. Pinon, P. et al. Talin-bound NPLY motif recruits integrin-signaling adapters to regulate cell
929 spreading and mechanosensing. *J Cell Biol* **205**, 265-81 (2014).
- 930 44. Wegener, K.L. et al. Structural basis of integrin activation by talin. *Cell* **128**, 171-82 (2007).
- 931 45. Cluzel, C. et al. The mechanisms and dynamics of (alpha)v(beta)3 integrin clustering in living
932 cells. *J Cell Biol* **171**, 383-92 (2005).
- 933 46. Hytonen, V.P. & Wehrle-Haller, B. Protein conformation as a regulator of cell-matrix
934 adhesion. *Phys Chem Chem Phys* **16**, 6342-57 (2014).

- 935 47. Wu, R. et al. Specificity of LIM domain interactions with receptor tyrosine kinases. *J Biol*
936 *Chem* **271**, 15934-41 (1996).
- 937 48. Wu, R.Y. & Gill, G.N. LIM domain recognition of a tyrosine-containing tight turn. *J Biol*
938 *Chem* **269**, 25085-90 (1994).
- 939 49. Pfaff, M. & Jurdic, P. Podosomes in osteoclast-like cells: structural analysis and cooperative
940 roles of paxillin, proline-rich tyrosine kinase 2 (Pyk2) and integrin alphaVbeta3. *J Cell Sci*
941 **114**, 2775-86 (2001).
- 942 50. Schaller, M.D., Otey, C.A., Hildebrand, J.D. & Parsons, J.T. Focal adhesion kinase and
943 paxillin bind to peptides mimicking beta integrin cytoplasmic domains. *J Cell Biol* **130**, 1181-
944 7 (1995).
- 945 51. Deakin, N.O. & Turner, C.E. Distinct roles for paxillin and Hic-5 in regulating breast cancer
946 cell morphology, invasion, and metastasis. *Mol Biol Cell* **22**, 327-41 (2011).
- 947 52. Kerppola, T.K. Bimolecular fluorescence complementation (BiFC) analysis as a probe of
948 protein interactions in living cells. *Annu Rev Biophys* **37**, 465-87 (2008).
- 949 53. Machiyama, H. et al. Displacement of p130Cas from focal adhesions links actomyosin
950 contraction to cell migration. *J Cell Sci* **127**, 3440-50 (2014).
- 951 54. Morell, M., Espargaro, A., Aviles, F.X. & Ventura, S. Detection of transient protein-protein
952 interactions by bimolecular fluorescence complementation: the Abl-SH3 case. *Proteomics* **7**,
953 1023-36 (2007).
- 954 55. Kuo, J.C., Han, X., Yates, J.R., 3rd & Waterman, C.M. Isolation of focal adhesion proteins
955 for biochemical and proteomic analysis. *Methods Mol Biol* **757**, 297-323 (2012).
- 956 56. Legerstee, K., Geverts, B., Slotman, J.A. & Houtsmuller, A.B. Dynamics and distribution of
957 paxillin, vinculin, zyxin and VASP depend on focal adhesion location and orientation. *Sci Rep*
958 **9**, 10460 (2019).
- 959 57. Choi, C.K., Zareno, J., Digman, M.A., Gratton, E. & Horwitz, A.R. Cross-correlated
960 fluctuation analysis reveals phosphorylation-regulated paxillin-FAK complexes in nascent
961 adhesions. *Biophys J* **100**, 583-592 (2011).
- 962 58. Turner, C.E. et al. Paxillin LD4 motif binds PAK and PIX through a novel 95-kD ankyrin
963 repeat, ARF-GAP protein: A role in cytoskeletal remodeling. *J Cell Biol* **145**, 851-63 (1999).
- 964 59. Turner, C.E., Glenney, J.R., Jr. & Burridge, K. Paxillin: a new vinculin-binding protein
965 present in focal adhesions. *J Cell Biol* **111**, 1059-68 (1990).
- 966 60. Parat, M.O. & Fox, P.L. Palmitoylation of caveolin-1 in endothelial cells is post-translational
967 but irreversible. *J Biol Chem* **276**, 15776-82 (2001).
- 968 61. Kanchanawong, P. et al. Nanoscale architecture of integrin-based cell adhesions. *Nature* **468**,
969 580-4 (2010).
- 970 62. Zlatkine, P., Mehul, B. & Magee, A.I. Retargeting of cytosolic proteins to the plasma
971 membrane by the Lck protein tyrosine kinase dual acylation motif. *J Cell Sci* **110** (Pt 5), 673-
972 9 (1997).
- 973 63. Bertolucci, C.M., Guibao, C.D. & Zheng, J. Structural features of the focal adhesion kinase-
974 paxillin complex give insight into the dynamics of focal adhesion assembly. *Protein Sci* **14**,
975 644-52 (2005).
- 976 64. Keeble, A.H. et al. Approaching infinite affinity through engineering of peptide-protein
977 interaction. *Proc Natl Acad Sci U S A* (2019).
- 978 65. Petit, M.M., Meulemans, S.M. & Van de Ven, W.J. The focal adhesion and nuclear targeting
979 capacity of the LIM-containing lipoma-preferred partner (LPP) protein. *J Biol Chem* **278**,
980 2157-68 (2003).
- 981 66. Eich, C. et al. Changes in membrane sphingolipid composition modulate dynamics and
982 adhesion of integrin nanoclusters. *Sci Rep* **6**, 20693 (2016).
- 983 67. Goksoy, E. et al. Structural basis for the autoinhibition of talin in regulating integrin
984 activation. *Mol Cell* **31**, 124-33 (2008).

985 68. Saltel, F. et al. New PI(4,5)P₂- and membrane proximal integrin-binding motifs in the talin
986 head control beta3-integrin clustering. *J Cell Biol* **187**, 715-31 (2009).

987 69. Liu, J. et al. Structural basis of phosphoinositide binding to kindlin-2 protein pleckstrin
988 homology domain in regulating integrin activation. *J Biol Chem* **286**, 43334-42 (2011).

989 70. Liu, Y., Zhu, Y., Ye, S. & Zhang, R. Crystal structure of kindlin-2 PH domain reveals a
990 conformational transition for its membrane anchoring and regulation of integrin activation.
991 *Protein Cell* **3**, 434-40 (2012).

992 71. Goni, G.M. et al. Phosphatidylinositol 4,5-bisphosphate triggers activation of focal adhesion
993 kinase by inducing clustering and conformational changes. *Proc Natl Acad Sci U S A* **111**,
994 E3177-86 (2014).

995 72. Herzog, F.A., Braun, L., Schoen, I. & Vogel, V. Structural Insights How PIP₂ Imposes
996 Preferred Binding Orientations of FAK at Lipid Membranes. *J Phys Chem B* **121**, 3523-3535
997 (2017).

998 73. Dong, J.M. et al. Proximity biotinylation provides insight into the molecular composition of
999 focal adhesions at the nanometer scale. *Sci Signal* **9**, rs4 (2016).

1000 74. Zaidel-Bar, R., Itzkovitz, S., Ma'ayan, A., Iyengar, R. & Geiger, B. Functional atlas of the
1001 integrin adhesome. *Nat Cell Biol* **9**, 858-67 (2007).

1002 75. Wolfenson, H. et al. A role for the juxtamembrane cytoplasm in the molecular dynamics of
1003 focal adhesions. *PLoS One* **4**, e4304 (2009).

1004 76. Farnebäck, G. *Two-Frame Motion Estimation Based on Polynomial Expansion*, 363-370
1005 (2003).

1006 77. Chertkova, A.O. et al. Robust and Bright Genetically Encoded Fluorescent Markers for
1007 Highlighting Structures and Compartments in Mammalian Cells. *bioRxiv*, 160374 (2020).

1008 78. Stutchbury, B., Atherton, P., Tsang, R., Wang, D.Y. & Ballestrem, C. Distinct focal adhesion
1009 protein modules control different aspects of mechanotransduction. *J Cell Sci* **130**, 1612-1624
1010 (2017).

1011

Figures

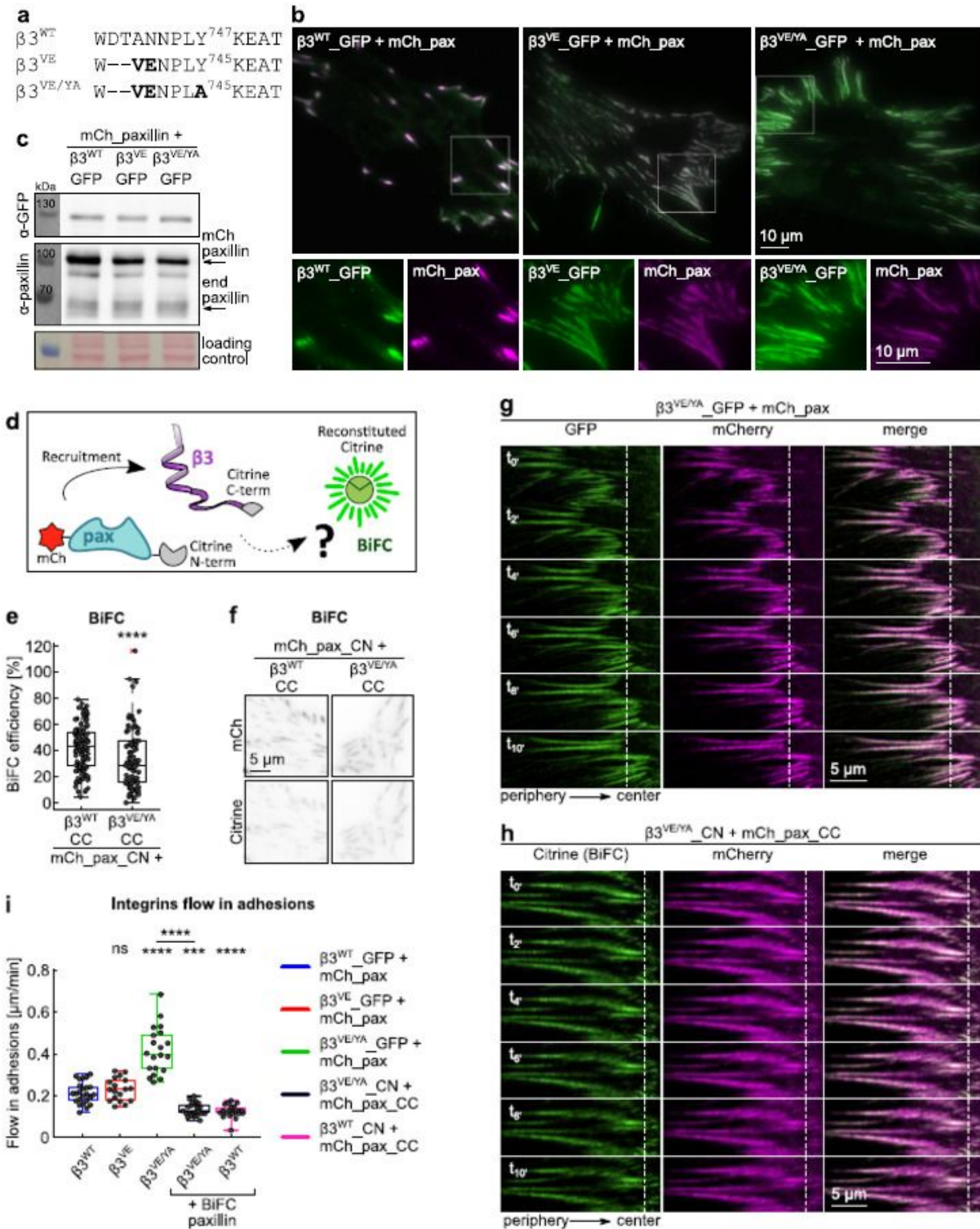


Figure 1

Morphology and dynamics of wild-type and mutant $\beta 3_{GFP}$ integrin-positive adhesions. (a) Sequence alignment of $\beta 3$ integrins, wt and mutants, at the NPLY747 motif. The high-affinity talin-binding chimeric $\beta 3$ integrins were obtained by introducing the VE motif from layilin. Bold indicates mutated residues. (b,c)

NIH-3T3 cells transiently transfected with $\beta 3$ _GFP integrins, wild-type or mutants, and mCherry_paxillin. (b) Representative TIRF images of cells fixed 24 hours after spreading on glass coverslips in serum containing medium and (c) recombinant protein expression assessed by western blotting against GFP and total paxillin. Loading control: Ponceau staining. (d) Schematic representation of the BiFC assay used to evaluate paxillin recruitment to $\beta 3$ integrins. (e,f) BiFC upon co-expression of mCherry_paxillin_CN and $\beta 3$ WT_CC or $\beta 3$ VE/YA_CC in NIH-3T3 fibroblasts. (e) Quantification of the BiFC efficiency. Statistical analysis is provided in Supplementary Table 1. (f) Representative TIRF images. (g,h) Kymographs representative of the displacement of $\beta 3$ VE/YA-containing adhesions, over a time period of 10 minutes, in the absence (g) and in the presence (h) of mechanically (BiFC) coupled paxillin. (i) Quantification of the $\beta 3$ integrins flow in adhesions, expressed as mean displacement over time ($\mu\text{m}/\text{min}$) per replicate. Statistical analysis is provided in Supplementary Table 2.

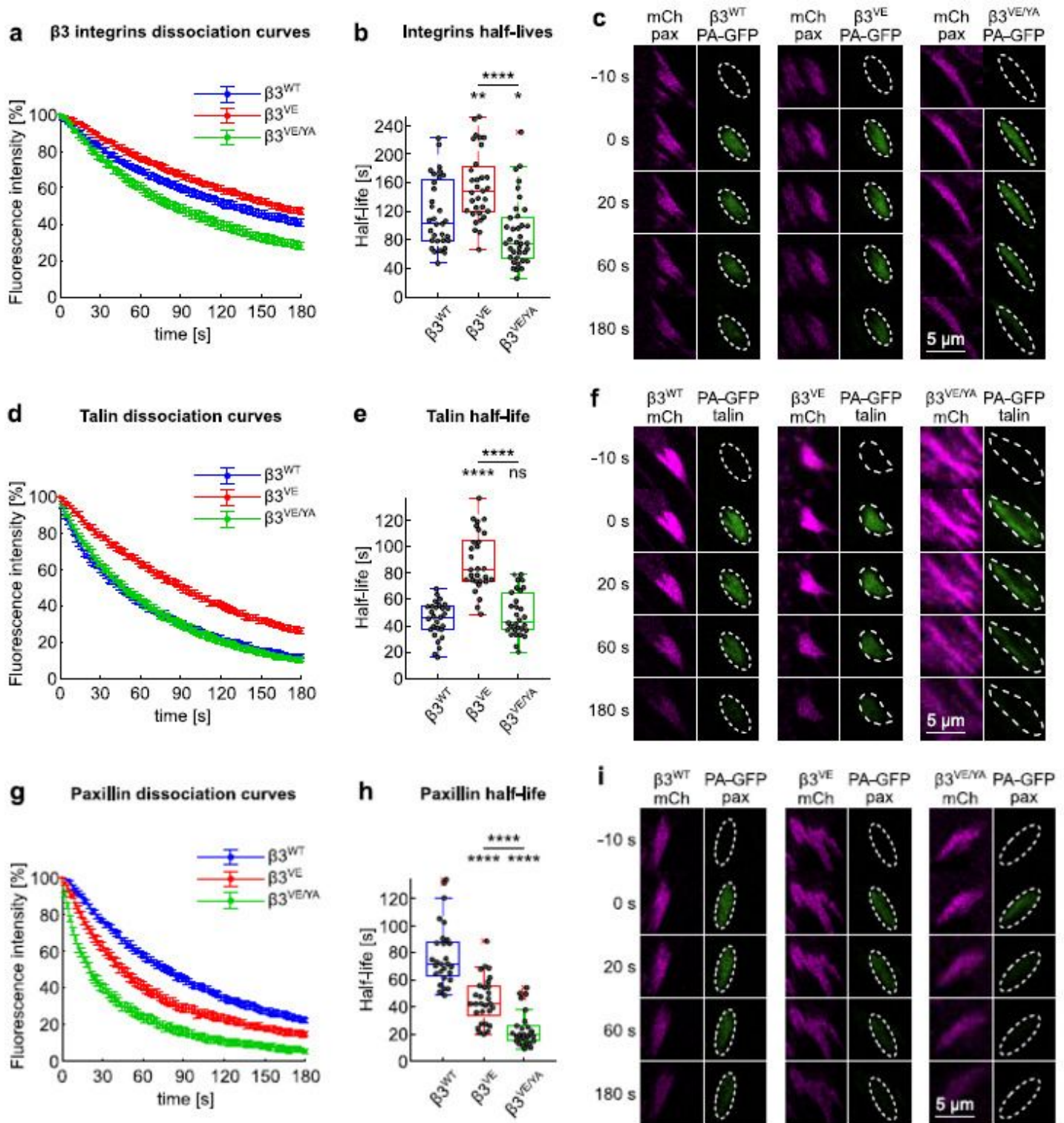


Figure 2

Analysis of the dissociation dynamics of the $\beta 3$ integrin/talin/paxillin complex. (a,d,g) Experimental dissociation curves of (a) $\beta 3$ _PA-GFP integrins from mCherry_paxillin-positive focal adhesions and of (d) PA-GFP_talin and (g) PA-GFP_paxillin from $\beta 3$ _mCherry-positive focal adhesions. (b,e,h) Box plot of the half-lives of (b) $\beta 3$ _PA-GFP integrins in mCherry_paxillin-positive FAs and of (e) PA-GFP_talin and (h) PA-

GFP_paxillin in $\beta 3_{\text{mCherry}}$ -positive FAs. Statistical analysis is provided in Supplementary Table 3. (c,f,i) Representative images of photoactivation time series of experiments in a-b, d-e and f-g.

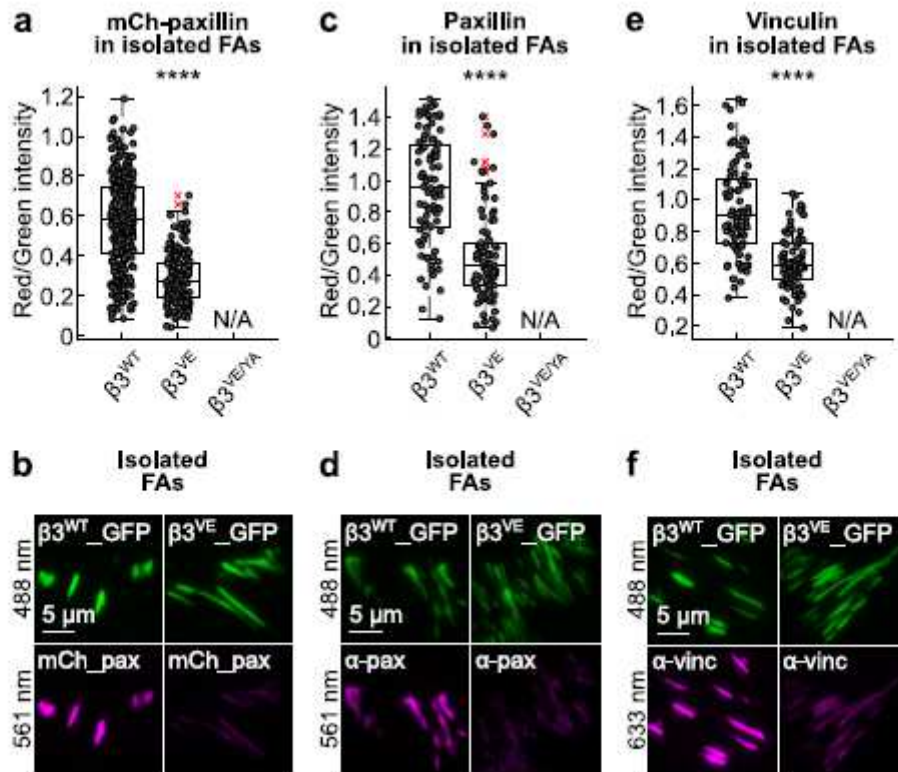


Figure 3

Analysis of paxillin and vinculin binding upon isolation of FA-complexes. (a,c,e) Quantification of cytoplasmic proteins retained in $\beta 3_{\text{WT_GFP}}$ - or $\beta 3_{\text{VE_GFP}}$ -positive FAs, isolated from NIH-3T3 fibroblasts. (a) mCh_paxillin, (c) endogenous paxillin and (e) endogenous vinculin. Statistical analysis is provided in Supplementary Table 4. (b,d,f) Representative TIRF images of FAs isolated from NIH-3T3 cells of experiments quantified in a, c and e.

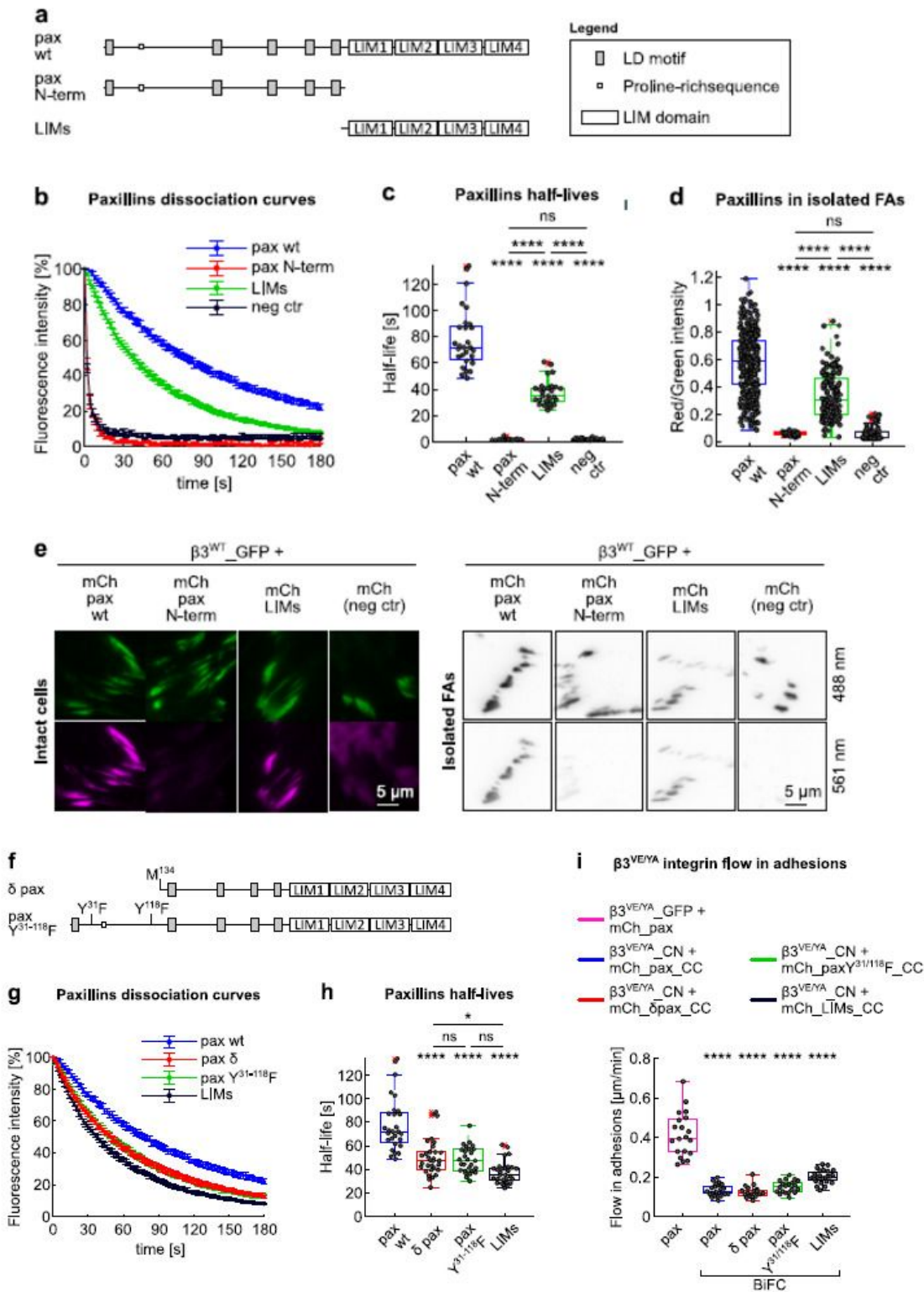


Figure 4

Paxillin binding to adhesions is driven by the LIM domains but stabilized by the N-terminus. (a,f) Schematic representation of paxillin (a) truncation mutants and (f) N-terminal mutants. All proteins were N-terminally tagged with PA-GFP or mCherry. (b,g) Experimental dissociation curves of PA-GFP_paxillin wt and (b) truncation mutants or (g) N-terminal mutants, from β_3 -mCherry-positive FAs. (c,h) Box plot of the half-life of PA-GFP_paxillin wt and (c) truncation mutants or (h) N-terminal mutants, in β_3 -mCherry-

positive FAs. Statistical analysis is provided in Supplementary Table 3. (d) Quantification of mCherry_paxillin wt and truncation mutants retained in FAs, isolated from NIH-3T3 cells co-expressing β 3WT_GFP. Statistical analysis is provided in Supplementary Table 4. (e) Representative TIRF images of FAs in NIH-3T3 cells co-expressing β 3WT_GFP and mCherry_paxillin proteins. Left panel: FAs in intact cells; right panel: isolated FAs. (i) Quantification of the β 3VE/YA integrin flow in adhesions, expressed as mean displacement over time ($\mu\text{m}/\text{min}$) per replicate. Statistical analysis is provided in Supplementary Table 2. Neg ctr: PA-GFP in photoactivation experiments and mCherry in isolated FAs.

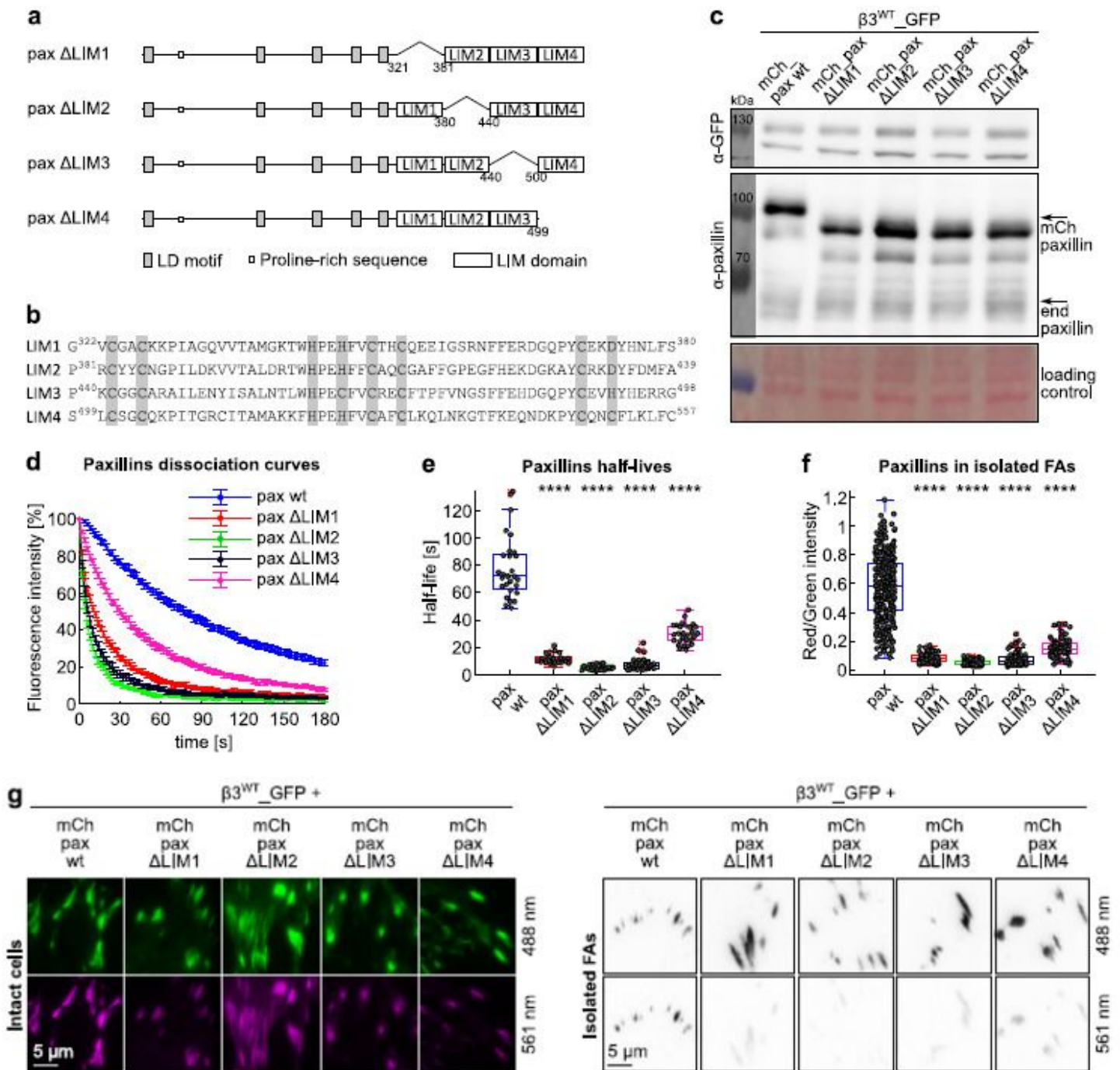


Figure 5

LIM domain deletion analysis by photoactivation and FA-isolation. (a) Schematic representation of the paxillin LIM domain deletion mutants. All proteins were N-terminally tagged with PA-GFP or mCherry. (b) Alignment of the four paxillin LIM domains. Grey: zinc-binding residues. (c) Western blot of protein extracts from NIH-3T3 fibroblasts transiently co-expressing β 3WT_GFP and mCherry-tagged paxillin proteins, wt or deletion mutants. Loading control: Ponceau staining. (d) Experimental dissociation curves of PA-GFP_paxillin wt and deletion mutants from β 3WT_mCherry-positive FAs. (e) Box plot of the corresponding half-lives. Statistical analysis is provided in Supplementary Table 3. (f) Quantification of mCherry_paxillin wt and mutants retained in FAs isolated from NIH-3T3 cells co-expressing β 3WT_GFP. Statistical analysis is provided in Supplementary Table 4. (g) Representative TIRF images of FAs in NIH-3T3 cells co-expressing β 3WT_GFP and mCherry_paxillin proteins. Left panel: FAs in intact cells; right panel: isolated FAs.

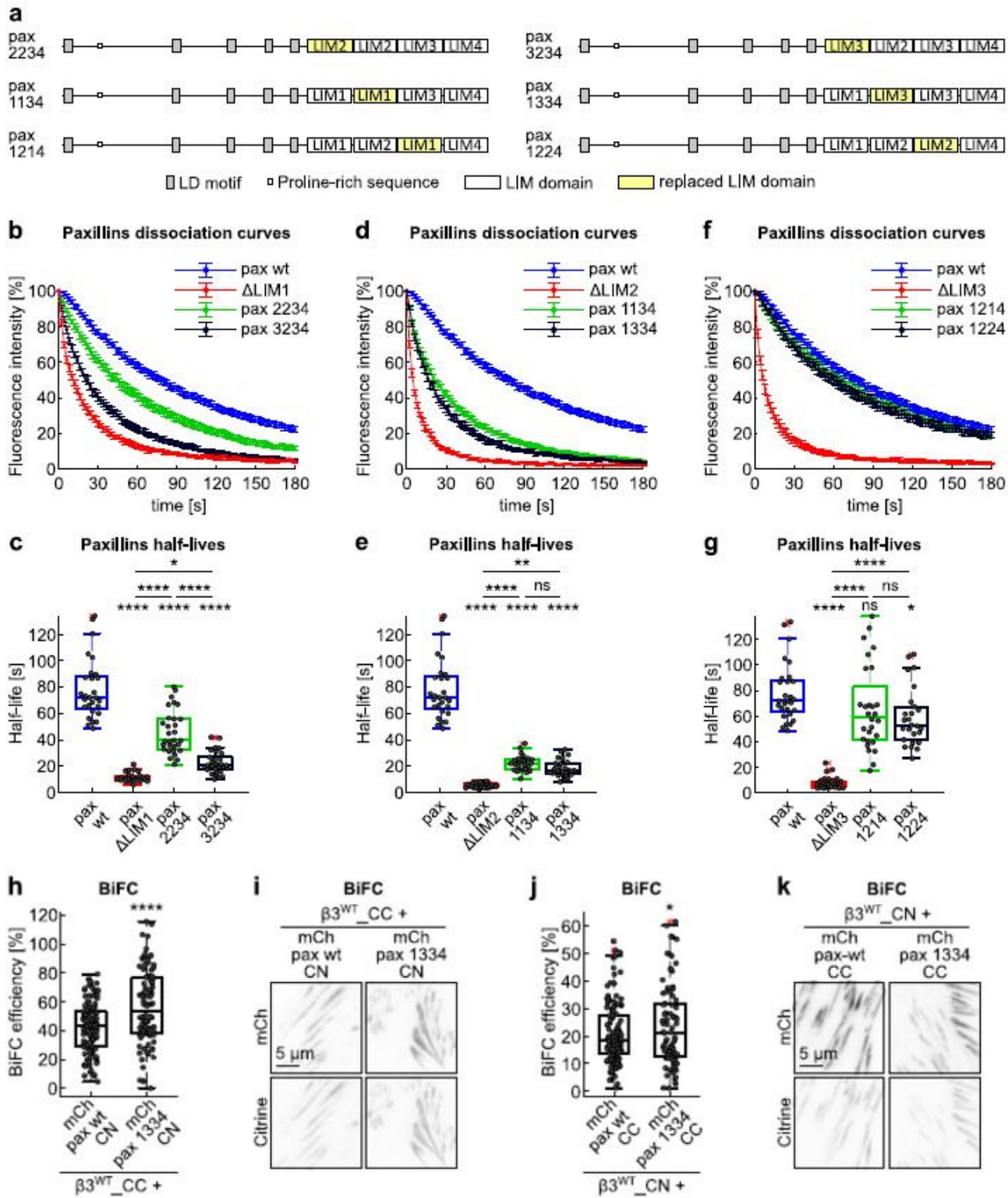


Figure 6

LIM domain-specific functions assessed by the LIM domain replacement strategy. (a) Schematic representation of the paxillin mutants obtained by the LIM domain replacement strategy. From the top line: replacement of LIM1, replacement of LIM2 and replacement of LIM3. All proteins were N-terminally tagged with PA-GFP. (b,d,f) Experimental dissociation curves of PA-GFP_paxillin wt and (b) LIM1 mutants, (d) LIM2 mutants and (f) LIM3 mutants, from β_3 mCherry-positive FAs. (c,e,g) Box plot of the half-lives

of PA-GFP_paxillin wt and (c) LIM1 mutants, (e) LIM2 mutants and (g) LIM3 mutants in $\beta 3$ _mCherry-positive FAs. Statistical analysis is provided in Supplementary Table 3. (h,i) BiFC upon co-expression of mCherry_paxillin_CN or its corresponding paxillin 1334 mutant and $\beta 3$ WT integrin C-terminally tagged with the citrine C-terminal fragment in NIH-3T3 cells. (h) Quantification of the BiFC efficiency. Statistical analysis is provided in Supplementary Table 1. (i) Representative TIRF images. (j,k) BiFC upon co-expression of mCherry_paxillin_CC or its corresponding paxillin 1334 mutant and $\beta 3$ WT integrin C-terminally tagged with the citrine N-terminal fragment in NIH-3T3 cells. (j) Quantification of the BiFC efficiency. Statistical analysis is provided in Supplementary Table 1. (k) Representative TIRF images.

a Conservation of the paxillin LIM4 domain across species

Species	Accession	Sequence	net charge
<i>H. sapiens</i>	PXN	CSGCGK P ITGRCITAMAK K FFH P EHFVCAFCL K QLNKGTF F KEQ N DKPYCQ N CFL K LF C	+5
<i>R. norvegicus</i>	PXN	CSGCG K PITGRCITAMAK K FFH P EHFVCAFCL K QLNKGTF F KEQ N DKPYCQ S CFL K LF C	+5
<i>M. musculus</i>	PXN	CSGCG K PITGRCITAMAK K FFH P EHFVCAFCL K QLNKGTF F KEQ N DKPYCQ S C F V K LF C	+5
<i>G. gallus</i>	PXN	CSGCG K PITGRCITAM G KK F FFH P EHFVCAFCL K QLNKGTF F KEQ N DKPYCQ N CFL K LF C	+5
<i>X. laevis</i>	PXN	CSGCG K PITGRCITAM G KK F FFH P EHFVCAFCL K QLNKGTF F KEQ N DKPYCQ N C F V K LF C	+5
<i>D. rerio</i>	PXNA	CSGCG K PITGRCITAM G KK F FFH P EHFVCAFCL K QLNKGTF F KEQ N DKPYCQ S C F V K LF S	+5
<i>D. melanogaster</i>	Pax	CAGCS K PITGRCITAM F KK F FFH P EHFVCAFCL K QLNKGTF F KEQ K DKPYC H T C F D K I F G	+5
<i>C. elegans</i>	PXL1	CS Q C R G A I N G R C V A A M G R K F F H P E H F R C S Y N H Q L T K G T F F K E V D R R P F C H K C Y N N T Y A L T P A	+6
<i>D. discoideum</i>	PAXB	CSGCG K A V S G R C V D A L D K K W H P E H F V C A F C M N P L A G G S Y T A N G K P Y C K G C H N K L F A	+3
LIM4 triple mutant		CSGCG K PIT G Q C ITAMAK K FFH P EHFVCAFCL E QLNKGTF F KEQ N DKPYCQ N CFL D LF C	0

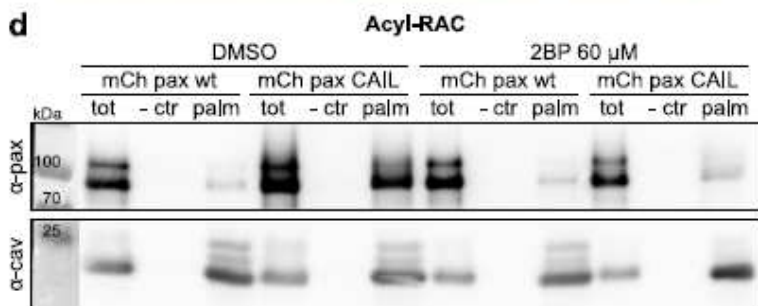
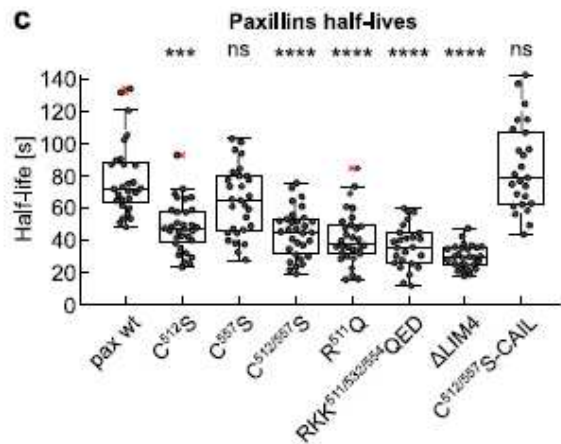
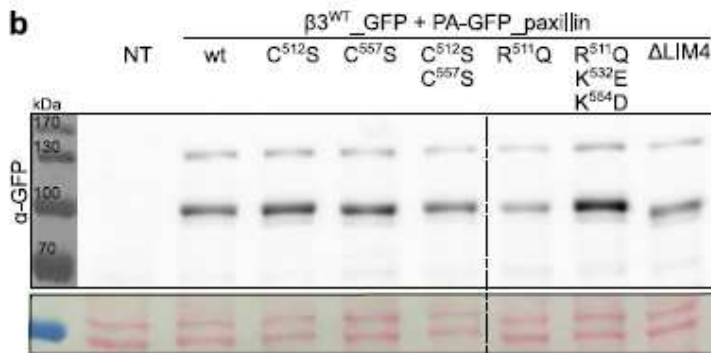


Figure 7

Paxillin LIM4 domain carries membrane binding features relevant for FA binding. (a) Alignment of the amino acid sequence of paxillin LIM4 across species and triple human paxillin LIM4 mutant (bottom). The latter was obtained by replacing three basic amino acids with neutral or acidic residues found at the corresponding positions in other paxillin LIM domains (RKK511/532/554QED). Grey: zinc-binding

residues; blue: positive residues; red: negative residues; bold: non-conserved residues in respect to the human paxillin LIM4 domain; arrows indicate the conserved free cysteines; yellow: conserved GRC motif. (b) Expression analysis, via western blot, of the paxillin LIM4 mutants. Loading control: Ponceau staining. (c) Box plot of the half-lives of PA-4GFP_paxillin wt and LIM4 mutants in β 3WT_mCherry-positive FAs. Statistical analysis is provided in Supplementary Table 3. (d) Acyl-Resin Assisted Capture assay from cell transiently transfected with mCherry_paxillin wt or mCherry_paxillin-CAIL, untreated (DMSO) or treated with 2-bromopalmitate. NT: not transfected; tot: total cell lysate; - ctr: negative control (tris-base); palm: fraction of palmitoylated proteins (hydroxylamine); 2BP: 2-bromopalmitate.

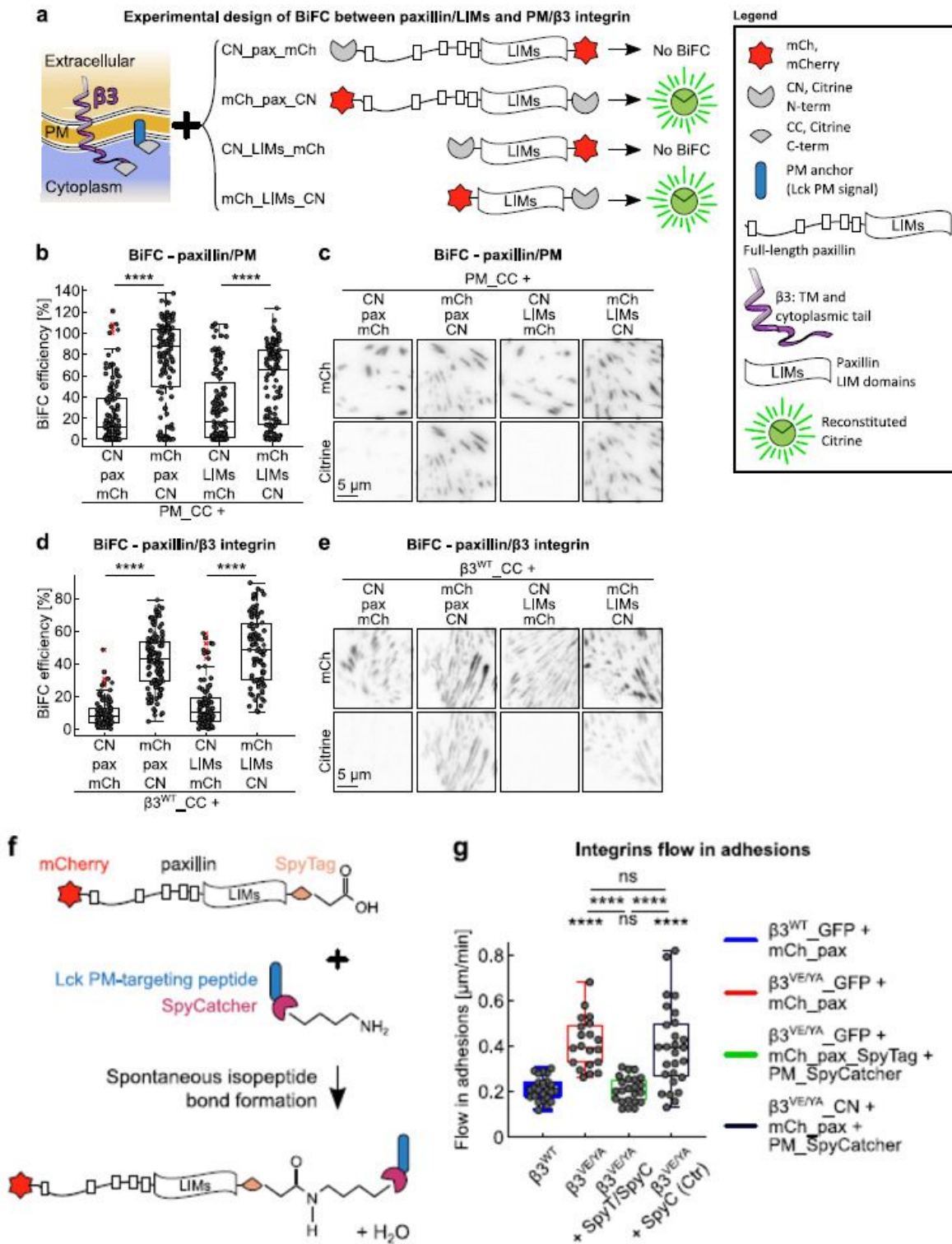


Figure 8

Preferential orientation of the paxillin LIM domains within FAs. (a) Overview of the molecules tested with the BiFC assays and a summary outcome, in terms of citrine fluorescence, of their pairwise expression. (b,d) Quantification of the BiFC signal generated by the co-expression of each of the paxillin constructs shown in figure a with (b) the plasma membrane-localized CC fragment, in Swiss-3T3 or with (d) the β 3^{WT} C-terminally tagged with CC, in NIH-3T3 cells. Statistical analysis is provided in Supplementary

Table 1. (c,e) Representative TIRF images of experiments quantified in b and d. (f) Schematic representation of the functioning SpyTag/SpyCatcher technology 64 and of how it has been used in our cellular system. (g) Quantification of the integrins flow in adhesions, expressed as mean displacement over time ($\mu\text{m}/\text{min}$) per replicate. Statistical analysis is provided in Supplementary Table 2.

Supplementary Files

This is a list of supplementary files associated with this preprint. Click to download.

- [Movie1.avi](#)
- [Movie2.avi](#)
- [Movie3.avi](#)
- [SupplementaryTables14.xlsx](#)
- [FigS1final.jpg](#)
- [FigS2final.jpg](#)
- [FigS3final.jpg](#)
- [FigS4final.jpg](#)